Reconciling lithospheric rheology between laboratory experiments, field observations and different tectonic settings

Ashley Bellas,[1] Shijie Zhong[1] and Anthony B. Watts[2]

[1]*Department of Physics, University of Colorado, Boulder, CO, 80302, USA. E-mail: ashley.bellas@colorado.edu*
[2]*Department of Earth Sciences, University of Oxford , United Kingdom, OX1 3AN*

SUMMARY

Recent modelling studies have shown that laboratory-derived rheology is too strong to reproduce observations of flexure at the Hawaiian Islands, while the same rheology appears consistent with outer rise—trench flexure at circum-Pacific subduction zones. Collectively, these results indicate that the rheology of an oceanic plate boundary is stronger than that of its interior, which, if correct, presents a challenge to understanding the formation of trenches and subduction initiation. To understand this dilemma, we first investigate laboratory-derived rheology using fully dynamic viscoelastic loading models and find that it is too strong to reproduce the observationally inferred elastic thickness, T_e, at most plate interior settings. The T_e can, however, be explained if the yield stress of low-temperature plasticity is significantly reduced, for example, by reducing the activation energy from 320 kJ mol^{-1}, as in Mei *et al.*, to 190 kJ mol^{-1} as was required by previous studies of the Hawaiian Islands, implying that the lithosphere beneath Hawaii is not anomalous. Second, we test the accuracy of the modelling methods used to constrain the rheology of subducting lithosphere, including the yield stress envelope (YSE) method, and the broken elastic plate model (BEPM). We show the YSE method accurately reproduces the model T_e to within ∼10 per cent error with only modest sensitivity to the assumed strain rate and curvature. Finally, we show that the response of a continuous plate is significantly enhanced when a free edge is introduced at or near an edge load, as in the BEPM, and is sensitive to the degree of viscous coupling at the free edge. Since subducting lithosphere is continuous and generally mechanically coupled to a sinking slab, the BEPM may falsely introduce a weakness and hence overestimate T_e at a trench because of trade-off. This could explain the results of recent modelling studies that suggest the rheology of subducting oceanic plate is stronger than that of its interior. However, further studies using more advanced thermal and mechanical models will be required in the future in order to quantify this.

Key words: Lithospheric flexure; Mechanics, theory, and modelling; Rheology: crust and lithosphere.

1 INTRODUCTION

Plate tectonics implies that the plates behave rigidly in the way they respond to loads on long geological timescales. The principal evidence for a rigid oceanic lithosphere has come from observations of flexure which show that the effective elastic thickness, T_e, (equivalent to flexural rigidity) increases with age away from a mid-ocean ridge (Watts 1978) and from experimental rock mechanics data which suggest that while its strength is limited by brittle deformation in its upper part and ductile flow in its lower part, the lithosphere has an intervening elastic 'core' that increases in thickness with age (Goetze & Evans 1979; Watts & Burov 2003). Recent studies based on modelling plate flexure [Hunter & Watts (2016) for circum-Pacific trench—outer rise systems and Zhong & Watts

(2013) for Hawaiian Islands] and low-temperature plasticity (LTP) laws (e.g. Mei *et al.* 2010) suggest, however, spatial variations in plate rigidity, with subduction zones appearing stronger than expected for the age of the plate at the time of loading and the interior of plates weaker. This poses a dilemma, especially for the formation of deep-sea trenches and the initiation of subduction, since plate boundaries would be expected to be generally weaker, not stronger, than plate interiors.

Possible explanations for this dilemma include consideration of the timescales of loading (Hunter & Watts 2016), the role of flexure-induced bending stresses (Craig *et al.* 2014a) and faulting (Billen & Gurnis 2005) and the thermal effects of magma-assisted flexure (Buck *et al.* 2015) due, for example, to 'petit' spots (Hirano *et al.* 2008) or deep mantle plumes (Pleus *et al.* 2020). Hunter &

Watts (2016), for example, found that while there is indeed evidence of a localized weak zone in the region of the seaward wall of a trench where the curvature of flexure is highest, the 'background' T_e of a trench—outer rise system (their so-called 'seaward T_e') was controlled by a relatively high (671–714 °C) oceanic isotherm compared to that found at the Hawaiian Islands (~450 °C). Similarly, McNutt (1984) found the mechanical thickness of subducting lithosphere to generally be larger than that at ocean island settings, and attributed the difference to regional thermal anomalies. However, there is increasing evidence to suggest that thermal rejuvenation by the Hawaiian plume does not significantly modify the lithospheric thermal structure (Ribe & Christensen 1994), surface heat flux (von Herzen 1989), nor does it support swell topography which appears to be dynamic (e.g. Ribe & Christensen 1994; Zhong & Watts 2002; Cadio *et al.* 2012; Huppert *et al.* 2020). Therefore, that estimates of T_e from recent studies indicate lithospheric rheology is stronger (i.e. higher yield stress) at subduction zones than at ocean island settings is not easily understood.

The purpose of this paper is to address this dilemma by a reevaluating some of the methods that have been used to model plate flexure and their implications for understanding the rheology of oceanic lithosphere in plate boundary and interior settings. Our focus is on the validity of broken elastic plate models (BEPM) and the yield stress envelope (YSE) methods used to estimate T_e, the sensitivity of these estimates to some of the parameters in laboratory-derived rheological laws, and the effects of regional variations in the thermal and/or magmatic structure on T_e. We use fully dynamic viscoelastic loading models to show that the YSE method accurately reproduces T_e and the state of stress of flexed oceanic lithosphere, and that the BEPM method significantly enhances the flexure such that a trade-off exists and an oceanic plate may appear stronger than it actually is, and that T_e at a majority of seamount and ocean-islands is overestimated by a factor of approximately 2 by laboratory-derived rheology.

2 MODELS AND METHODS

In this section, we present lithospheric rheology including brittle and ductile yielding mechanisms. We then introduce the YSE method and the numerical viscoelastic loading model. The elastic plate model (EPM) and BEPM are well documented in previous studies and so are reproduced here only visually (Fig. 1, for full details, refer to Turcotte & Schubert 1982, or Watts 2001). The lithosphere may be approximated to first order as an elastic plate, but more complete models include the possibility for anelastic yielding that may occur under high stress and high temperature conditions.

2.1 Lithospheric rheology

Laboratory studies suggest that when stress exceeds the local elastic limit, anelastic yielding of the lithosphere is controlled by (i) frictional sliding, (ii) LTP (also commonly referred to as dislocation glide or Peierls creep) and (iii) high-temperature creep (HTC). The yield stress of frictional sliding is formulated (Byerlee 1978)

$$\tau_{\text{yield}} = \mu_f \rho g z, \tag{1}$$

in which μ_f is the frictional coefficient of a pre-existing fault, ρ is density, g acceleration due to gravity and z is depth. This simple formulation assumes that the normal stress on an arbitrary fault is equal to the local lithostatic pressure, although it is also straightforward to consider the differing normal stress and strength of normal,
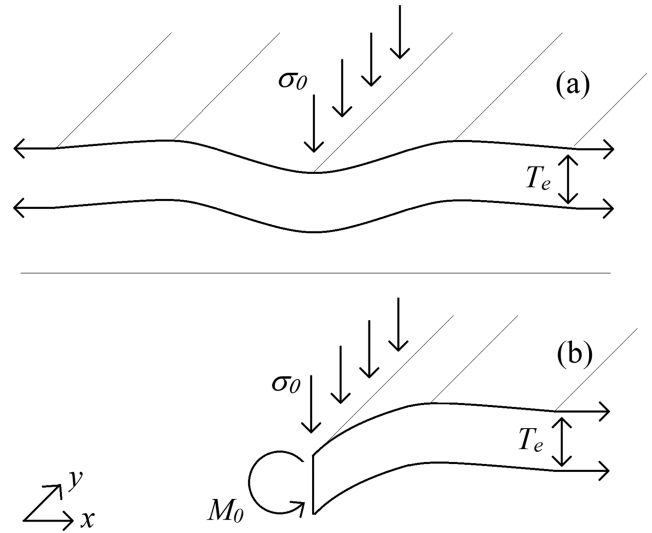

Figure 1. Schematics of the EPM and the BEPM. (a) The EPM is infinite in 2-D space. The plate is assumed to be thin relative to the width or wavelength of the load such that vertical variations within the plate can be neglected. The load pictured is an infinite line load or delta function in *x*, and constant in *y*. Commonly used loads also include sinusoidal loads and finite-width loads. (b) The BEPM is identical to the EPM except that the model geometry is semi-infinite in *x* and a bending moment is often applied to the free edge. The deformational response in both the EPM and the BEPM is purely elastic.

reverse and strike-slip faults. While the seminal laboratory study of Byerlee (1978) estimated the frictional coefficient $\mu_f = 0.7$, observational and modelling studies estimate $\mu_f = 0.3$ based on the dip angle newly formed faults in the outer-rise at subduction zones (Craig *et al.* 2014b), as well as based on the seismic strain rate at the Hawaiian Islands (Bellas & Zhong 2021). Based on observations of heat flux above interplate thrust faults, $\mu_f < 0.1$ (Gao & Wang 2014; England 2018). The reasons for this spread in μ_f between different tectonic settings and laboratory conditions are not generally understood.

LTP (i.e. dislocation glide or Peierls creep) is formulated (e.g. Mei *et al.* 2010)

$$\dot{\epsilon} = A\sigma^n \exp\left(-\frac{E_p}{RT}\left(1 - \left(\frac{\sigma}{\sigma_P}\right)^p\right)^q\right), \tag{2}$$

in which $\dot{\epsilon}$ and σ are the second invariants of the strain rate and deviatoric stress tensors, respectively, *A* is the pre-exponential factor, *n* is a constant, E_p is the plastic activation energy, *R* is the gas constant, *T* is temperature, σ_P is the Peierls stress and *p* and *q* are constants determined in experiments (Figs 2a and b). Different laboratory studies estimate significantly different parameter values which may be resolved by considering the length scales of deformation (Kumamoto *et al.* 2017). However, even the weakest of laboratory-derived LTP flow laws (Idrissi *et al.* 2016) is too strong to reproduce observations of flexure at the Hawaiian Islands (Zhong & Watts 2013; Bellas *et al.* 2020). Zhong & Watts (2013) showed that the flexural strength of the lithosphere is controlled to first order by LTP, and so this deformation mechanism is of greatest importance in the following work.

HTC including diffusion and dislocation creep may be formulated as a composite law (e.g. Podolefsky *et al.* 2004; Zhong & Watts 2013)

$$\dot{\epsilon} = B\sigma \left(\sigma_T^{m-1} + \sigma^{m-1}\right) \exp\left(-\frac{E_c}{RT} + \frac{E_c}{RT_m}\right), \tag{3}$$
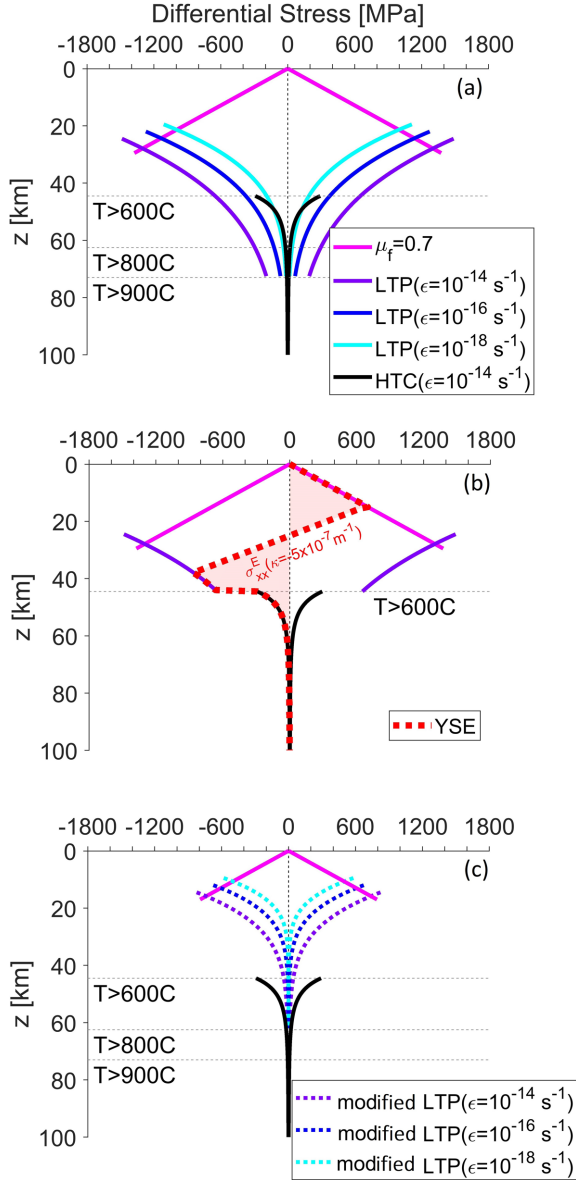
Figure 2. Lithospheric rheology and the YSE. The YSE represents lithospheric strength as a function of depth in terms of the maximum stress, σ_{xx}, that can be supported at each depth. A 90 Ma thermal structure is assumed in all panels based on the half-space cooling model. (a) The YSE based on laboratory-derived rheology for frictional sliding (μ_f), LTP and HTC. (b) Same as (a), except the intersection of elastic bending stresses (dashed red) with the YSE is shown. (c) Same as (a), except the activation energy of LTP is reduced from 320 to 190 kJ mol^{-1} as is required to reproduce observations of flexure at the Hawaiian Islands (Zhong & Watts 2013; Bellas et al. 2020).

Table 1. Model parameters.

Parameter	Value
Shear modulus, μ	3.3333×10^{10} Pa
Reference viscosity, η_0	10^{20} Pa s
Gravitational acceleration, g	10 m s^{-2}
Gas constant, R	8.32 J (mol K)$^{-1}$
Mantle density, ρ	3330 kg m^{-3}
Mantle temperature, T_m	$1350\,°C$

Frictional sliding (Byerlee 1978)	
$\eta = \frac{\sigma}{2\dot{\epsilon}} = \frac{\tau_{\text{yield}}}{\dot{\epsilon}} = \frac{\mu_f \sigma_n}{\dot{\epsilon}}$	
*Frictional coefficient, μ_f	0.7

Low-temperature plasticity (Mei et al. 2010)	
$\eta = \frac{\sigma}{2\dot{\epsilon}} = \frac{\sigma^{1-n}}{A} \exp\{\frac{E_p}{RT}[1 - (\frac{\sigma}{\sigma_P})^p]^q\}$	
Pre-exponential factor, A	1.4×10^{-7} MPa^{-2}
*Activation energy, E_p	320 kJ mol^{-1}
Peierls stress, σ_P	5.9 GPa
Stress exponent, n	2
Stress exponent, p	1/2
Stress exponent, q	2

High-temperature creep (Podolefsky et al. 2004)	
$\eta = \frac{\sigma}{2\dot{\epsilon}} = \frac{\eta_0}{1+(\sigma/\sigma_T)^{m-1}} \exp(\frac{E_c}{RT} - \frac{E_c}{RT_m})$	
Stress exponent, m	3.5
Transition stress, σ_T	3×10^5 Pa
Activation energy, E_c	360 kJ mol^{-1}
*Activation temperature, T_{HTC}	$800\,°C$

*Parameters marked with an asterisk are varied to test their influence on flexure. Note that although the reference viscosity is 10^{20} Pa s, a minimum viscosity of 10^{21} Pa s is imposed in numerical models.

rebound (e.g. Mitrovica & Forte 1997), and post-seismic deformation (e.g. Freed et al. 2010) and does not have a strong influence on flexure (Zhong & Watts 2013).

In Fig. 2(a), we show the yield stress envelope (YSE) defined by these three deformation mechanisms. Macroscopic yielding occurs when stress exceeds the local yield stress, while stress below the local yield stress causes elastic deformation (Fig. 2b). The yield stress associated with each deformation mechanism is solved from constitutive eqs (1–3) by assuming either a strain rate and a temperature profile (LTP and HTC) or increasing lithostatic pressure with depth (frictional sliding).

2.2 The yield stress envelope method

The YSE method asserts that the effective elastic thickness, T_e, of a yielding plate can be defined based on the bending moment at a given curvature (McNutt & Menard 1982). The bending moment of a yielding plate can be calculated from the general expression of the bending moment,

$$M_0 = \int \sigma_{xx} (z - z_n) \, dz, \quad (4)$$

in which σ_{xx} is the differential stress due to flexure, z is depth and z_n is depth to the neutral plane in the flexed plate. Note that the differential stress in a yielding plate is given by the elastic bending stress truncated by the YSE, where the elastic bending stress is expressed

$$\sigma_{xx} = \frac{\kappa E (z - z_n)}{1 - \nu^2}, \quad (5)$$

in which κ is curvature, E is Young's modulus and ν is Poisson's ratio. Note also that the total stress component $\sigma_{zz} = 0$ such that differential stress is given by σ_{xx}.

in which B is a pre-exponential factor, σ_T is the transition stress at which diffusion and dislocation creep contribute equally to strain rate, m is a constant, E_c is the HTC activation energy which we assume to be equal for diffusion and dislocation creep for simplicity and T_m is the reference mantle temperature. The parameter values for HTC used in this study reproduce observations of seismic anisotropy in geodynamic models (Podolefsky et al. 2004) (Table 1). HTC is generally well understood from laboratory studies (Karato & Wu 1993; Hirth & Kohlstedt 2003), studies of the long-wavelength geoid (e.g. Hager & Richards 1989), postglacial

The intersection of the elastic bending stress with the YSE (i.e. the integrand in eq. 4) is presented in Fig. 2(b). To solve T_e of a yielding plate, the bending moment of the yielding plate (eq. 4, Fig. 2b) is equated to the bending moment of a purely elastic plate, which is expressed

$$M_0 = \frac{\kappa E}{12(1-\nu^2)} T_e^3 . \tag{6}$$

It is worth noting here that the YSE method is generally applied with numerous approximations and simplifications. For example, the YSE is typically solved for a constant values of strain rate, curvature, neutral plane depth, although they may vary significantly in time and space. Previous work has shown that the YSE method is most accurate when the maximum curvature is chosen (Mueller & Phillips 1995), but we will perform a test of this method against fully dynamic models for the first time here.

2.3 The viscoelastic loading model

Viscoelastic loading models are fully dynamic, meaning they account for spatial and temporal variations in stress, strain rate, curvature, etc. Comparing the fully dynamic solutions with those of the YSE method will allow us to test whether these spatial variations are necessary to resolve for an accurate estimate of elastic thickness. We will also use the viscoelastic loading model to investigate the efficacy of applying the BEPM to model flexure at subduction zones.

Deformation of an incompressible viscoelastic medium is expressed by the conservation equations of mass and momentum (e.g. Zhong & Watts 2013)

$$u_{i,i} = 0, \tag{7}$$

$$\sigma_{ij,j} - (\rho g u_3)_{,i} = 0, \tag{8}$$

in which u_i is the displacement, σ_{ij} is the stress tensor, ρ density, g acceleration due to gravity and subscripts after a comma denote a spatial derivative. The constitutive equation of a Maxwellian medium is

$$\sigma_{ij} + \frac{\eta}{\mu} \dot{\sigma}_{ij} = -p\delta_{ij} - 2\eta\dot{\epsilon}_{ij}, \tag{9}$$

in which η is the viscosity, μ the shear modulus, $\dot{\sigma}_{ij}$ the stress rate tensor, p pressure and $\dot{\epsilon}_{ij}$ the strain rate tensor. Maxwellian rheology represents viscous and elastic deformation combined in series (e.g. Zhong *et al.* 2003). An important timescale for viscoelastic deformation is given by the Maxwell time, $\tau_M = \eta/\mu$ (e.g. $\sim$950 yr for $\eta = 10^{21}$ Pa s), which is the characteristic timescale on which viscoelastic deformation occurs.

In the numerical models, the viscosity field is defined in one of three major ways to emulate and test the YSE method and BEPM. First, and most simply, viscosity may be bimodal with two vertically stratified layers (e.g. Fig. 3b). In two-layer models, a high-viscosity plate (10^{27} Pa s) overlies a low-viscosity mantle (10^{21} Pa s). This two-layer viscosity structure simulates an elastic plate with thickness equal to that of the high-viscosity plate because essentially zero viscous stress relaxation occurs in the high-viscosity layer on the timescales relevant to flexure. Therefore, the high-viscosity plate is effectively a purely elastic plate, and this has been demonstrated in benchmark calculations with the EPM in previous work (e.g. Zhong 1997; Zhong & Watts 2013).

Second, viscosity may be defined based on the laboratory-derived constitutive eqs (1–3) and the relationship $\eta=\sigma/2\dot{\epsilon}$ to test the YSE
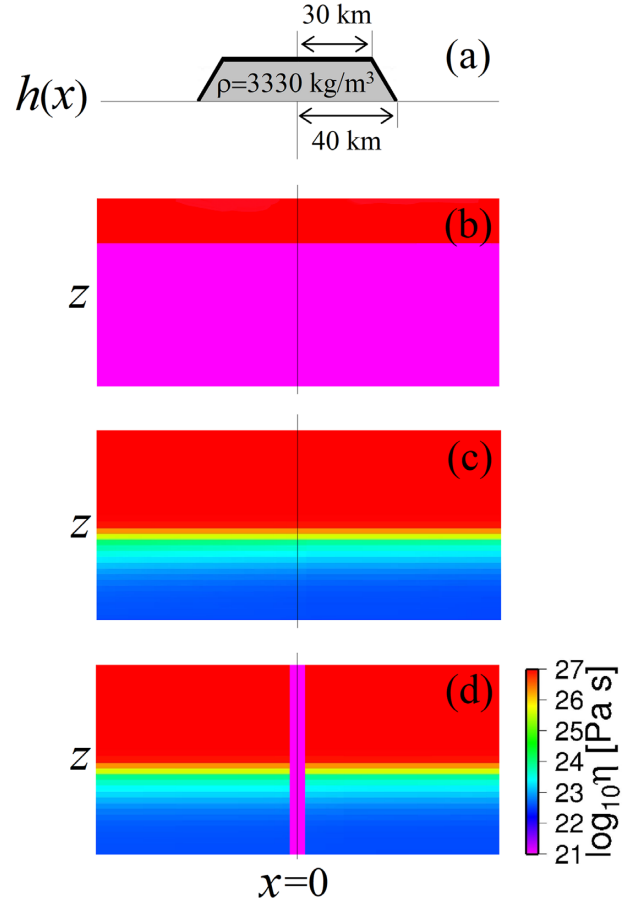

Figure 3. Schematic of viscoelastic loading models. We present the load and examples of the three main viscosity structures that are assigned in 2-D viscoelastic loading models (not to scale). (a) The load is applied to the surface boundary as a normal stress related to topography following $\sigma_0=\rho g h(x)$. Viscoelastic loading models are configured either with two-layer viscosity (b), with viscosity based on laboratory studies (c), or with viscosity based on laboratory studies and an imposed weak zone of finite width centred on $x = 0$ (d). The shear modulus throughout the domain is uniform. Note that the models are configured with a reflecting boundary condition at $x = 0$. In all other figures, only results on the right-hand side of $x = 0$ are presented, across which results are symmetric.

method (Fig. 3c). In the models, viscosity is defined by HTC (eq. 3) wherever temperature exceeds an imposed activation temperature, T_{HTC}. The activation temperature is varied from 600 °C to 900 °C in our study, a range which is approximately centered on the value recommended by laboratory studies of 800 °C (Mei *et al.* 2010). It is important to impose T_{HTC} because HTC is limited by diffusional processes on the microscale, which are activated by thermal energy. In particular, diffusion creep is limited by diffusion of grain boundaries, and dislocation creep is limited by the diffusion of dislocations and/or crystallographic defects (i.e. the climb velocity of jogs, Mei *et al.* 2010; Karato 2012). Wherever temperature is less than T_{HTC}, the viscosity is defined by the lower of those predicted by frictional sliding and LTP (e.g. Fig. 3c).

Third, viscosity may be defined based on laboratory-derived constitutive eqs (1–3) and with a low-viscosity zone imposed near $x = 0$ to the test the BEPM (e.g. Fig. 3d). Imposing such a weak zone allows us to simulate a free edge, because the lithospheric plate is effectively free and decoupled near $x = 0$. We aim to configure a fully dynamic model with effectively semi-infinite geometry and

a free edge as in the BEPM to test the implications of the BEPM when it is applied to model flexure at subduction zones.

The key motivation behind the numerical model setups is to estimate the effective elastic thickness, T_e, of a complex viscosity lithosphere. To estimate T_e, we compare the steady-state flexure from a complex viscosity model with many two-layer models for which the high-viscosity layer thickness (T_e) is varied in 1 km increments. Then, the T_e of the complex viscosity model is given by the two-layer model which best-reproduces the steady-state flexure. This methodology accounts for spatial variations in strain rate, stress, curvature etc., which will allow us to test whether simplified methods such as the YSE and BEPM accurately account for these variations based on their estimates of T_e. In addition, since the numerical models are used only to estimate T_e and we do not compare predictions with observed flexural profiles, we are afforded several simplifications. In particular, T_e is either completely insensitive or weakly sensitive to the load for linear and nonlinear rheology, respectively (refer to Section 3.1), and we neglect infill of the flexural depression by sediment or rocks and the weight of water, although results are not appreciably changed compared to previous work which included these effects (e.g. Bellas *et al.* 2020).

We assume a load that is constant in time and imposed as a normal stress on the surface boundary (Fig. 3a). The load is trapezoidal in shape with bottom-half-width equal to 40 km, top-half-width equal to 30 km, height equal to 3 or 6 km, and the normal stress corresponds to local topography and mantle density following $\sigma_0 = \rho g h(x)$, where $h(x)$ is the topography of the load (Fig. 3). Since the load is imposed as a normal stress on the surface and the weight of water is neglected, a surface load with 3 km height and mantle density corresponds to a load of 5.3 km height and 2900 kg m^{-3} density (i.e. that of intrusive mafic rocks, Watts *et al.* 2021) when the weight of water is considered. Similarly, a load with 6 km height in our simplified models corresponds to a seamount with 10.6 km height, and we suggest that these load choices adequately represent the observed spread in seamount heights around the globe.

The governing equations are solved using a finite-element model, CitcomSVE, that was originally developed for modelling glacial isostatic adjustment in a spherical shell geometry (Zhong *et al.* 2003) and later modified to include nonlinear rheology and Cartesian geometry (Zhong & Watts 2013). All numerical models in this study have 2-D Cartesian geometry, uniform mantle density and uniform elastic properties. The vertical sidewall and bottom boundary conditions are free-slip (i.e. reflecting), and the surface boundary is a free and deformable surface (i.e. stress-free). The reflecting boundary conditions allow models to simulate loading in a domain that is effectively infinite in the horizontal dimension. The model domain is 1500 km wide (x), and 600 km deep (z) with 256 horizontal elements and 160 vertical elements. Horizontal grid refinement is applied near the load, such that the horizontal resolution is 2 km at $x = 0$ km and increases linearly to 10 km at $x = 1500$ km. The vertical resolution is 2.5 km in the upper 100 km and 4.2 km in the lower 500 km in all complex viscosity models. In two-layer viscosity models, the vertical resolution is 3–4 km in the high-viscosity layer. Numerical models are evolved in time with time steps equal to a quarter Maxwell time, $\tau_M/4 \sim 238$ yr. Note that all model results are symmetric across $x = 0$.

3 RESULTS

Results are presented in three major sections. First, in Section 3.1, we predict T_e based on laboratory-derived rheology for a broad range of parameter values and compare predictions with observations. Second, in Section 3.2, we test whether the YSE method accurately reproduces the T_e of fully dynamic viscoelastic loading models. Third, in Section 3.3, we investigate the effects of introducing a free edge in models of flexure as is done in the BEPM. Finally, in Appendix A, interested readers will find an analysis of the type of error that arises in the classic EPM when the thin plate approximation breaks down.

3.1 Laboratory-derived lithospheric rheology and global observations of flexure

It has been suggested that the Hawaiian lithosphere may be weaker than laboratory-derived rheology would predict (Zhong & Watts 2013; Hunter & Watts 2016; Bellas *et al.* 2020) because it is thermomechanically eroded by the Hawaiian plume (e.g. Hunter & Watts 2016; Pleus *et al.* 2020), and/or due to magmatic diking and intrusion (Buck *et al.* 2015). Hypothetically, if the discrepancy between the observed and predicted flexure at the Hawaiian Islands is indeed caused by thermal and/or magmatic anomalies, then we expect that laboratory-derived lithospheric rheology would more accurately reproduce flexure elsewhere, for example, at ocean-island settings where plume activity and volcanism are not as extensive such as Bermuda, Cape Verde, the Island of Mayotte, or the Canary Islands. We would consider it highly unlikely for mantle plumes, magmatic diking and intrusion to modify the lithosphere to equal degree at many seamounts and ocean islands with much weaker plume activity and volcanism than that at the Hawaiian Islands. In contrast, if the source of the discrepancy is that laboratory-derived rheology is too strong, then laboratory-derived rheology should repeatedly underestimate flexure at many ocean island settings to approximately equal degree no matter the extent of plume activity and volcanism. To discriminate between these possibilities, we formulate viscoelastic loading models with a broad range of lithospheric thermal ages and load amplitudes (e.g. Fig. 4) and compare with a global observational data set of elastic thickness, T_e (Fig. 5).

In the viscoelastic loading models, lithospheric thermal age is varied from 20 to 130 Ma in 10 Ma increments, and the thermal structure is calculated using the half-space cooling model. The time-dependent flexural response to the load is computed for 500 Maxwell times to a steady-state ($\sim$475 kyr, $\tau_M = \eta_0/\mu$). In Case 1 h, which belongs to Suite 1, the thermal age is 90 Ma, the frictional coefficient is $\mu_f = 0.7$, LTP is defined exactly as derived by the laboratory study of Mei *et al.* (2010), HTC is formulated following Zhong & Watts (2013), and we set the activation temperature $T_{HTC} = 800\,°C$ (Tables 1 and 2). The evolution of surface flexure, internal viscosity, stress and strain fields are shown at $t = 0$ (Figs 4a–d), $t = 12.5\tau_M$ (Figs 4e–h) and $t = 500\tau_M$ (Figs 4i–l). At $t = 500\tau_M$, surface flexure is maximal (Fig. 4i), the lithosphere is thinned beneath the load due to nonlinear weakening (Fig. 4j), the load is supported by lithospheric stress (Fig. 4k) and the strain rate is negligible indicating a steady state (Fig. 4l). The steady-state surface flexure is best-reproduced by a two-layer model with $T_e = 64$ km which indicates that T_e of the complex viscoelastic lithosphere in Case 1h is 64 km (Figs 4m–p). We note that $T_e = 64$ km would be unusually high for 90 Ma oceanic lithosphere.

In Suite 1, we compute the evolution of a suite of models that are identical to Case 1h except the age of the lithosphere is varied in 10 Ma increments from 20 to 130 Ma. The predictions of T_e from Suite 1 approximately follow the 800 °C isotherm, which increases from $\sim$25 km depth at 20 Ma, to $\sim$80 km depth at 130 Ma (Fig. 5b,
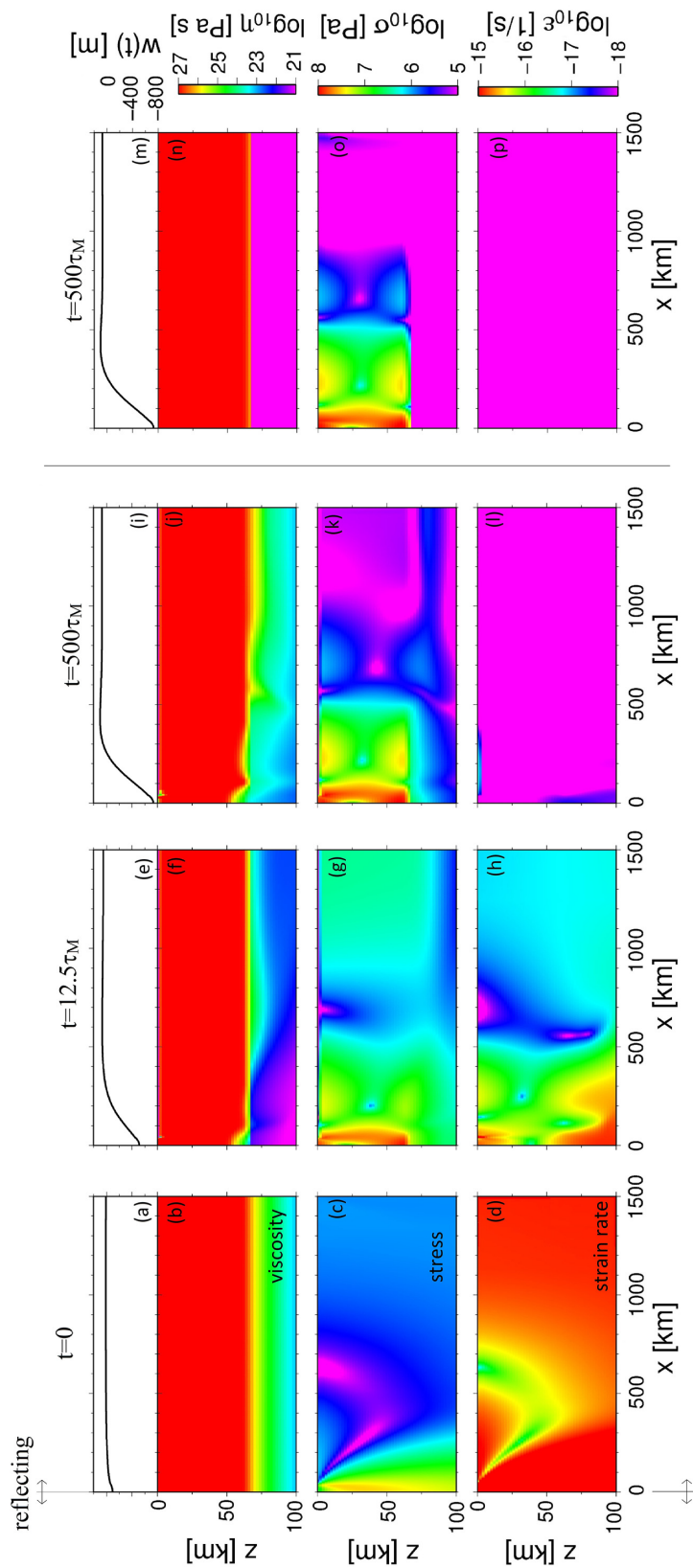
Figure 4. Time evolution of Case 1h and a snapshot of the best-fitting two-layer model. Note that only half of the flexural profile or field is pictured here (results are reflected across $x = 0$), and only the upper 100 km of the domain is shown, though it is 600 km deep. (a)–(d) At $t = 0$, the response of the system is purely elastic. (e)–(h) When time has reached $t = 12.5\tau_M$, viscous relaxation has caused stress to concentrate in the lithosphere near the load, and strain to concentrate in the shallow lithosphere and weak underlying mantle near the load. (i)–(l) When time has reached $t = 500\tau_M$, the system has reached steady state. (m)–(p) When time has reached $t = 500\tau_M$, the system has reached steady state. The best fit to steady-state flexure is produced by a two-layer model with $T_e = 64$ km.
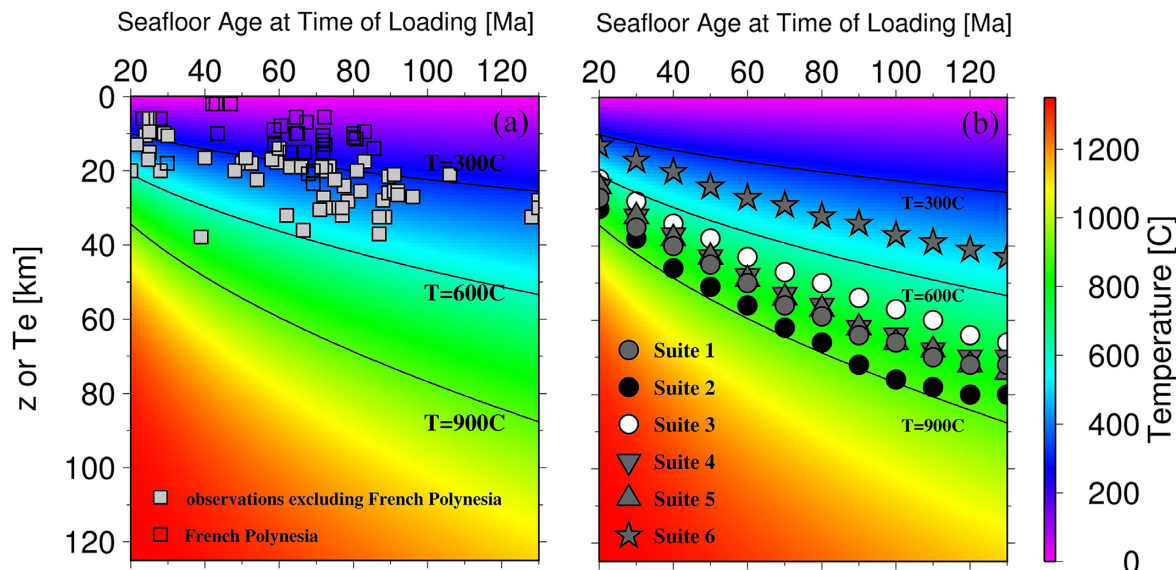
Figure 5. Observed and predicted elastic thickness, T_e. Observed (a) and predicted (b) elastic thickness as a function of seafloor age supposed on a colour map which shows the thermal structure based on the half-space cooling model. Black lines show isotherms for 300 °C, 600 °C and 900 °C. In Suite 1, $\mu_f = 0.7$, $E_{LTP} = 320\,\mathrm{kJ\,mol^{-1}}$, $A_0 = 3$ km and $T_{HTC} = 800$ °C where μ_f is the frictional coefficient, E_{LTP} is the activation energy of low-temperature plasticity, A_0 is the trapezoidal load amplitude and T_{HTC} is the activation temperature for HTC. All other suites are identical to Suite 1 except for the following modifications. In Suite 2, T_{HTC} is increased to 900 °C. In Suite 3, T_{HTC} is decreased to 600 °C. In Suite 4, A_0 is increased to 6 km. In Suite 5, μ_f is decreased to 0.3. In Suite 6, E_{LTP} is decreased to 190 kJ mol^{-1}.

Table 2). Note that we have set the threshold temperature $T_{HTC} = 800$ °C.

We increase $T_{HTC} = 900$ °C in Suite 2 and leave all other parameters unchanged relative to Suite 1. In Suite 2, the T_e approximately follows the 900 °C isotherm (Fig. 5b and Table 2). The reason for which T_e approximately follows the isotherm of T_{HTC} in Suites 1 and 2 is made clear by Fig. 2(a), where laboratory-derived rheology predicts a large yield stress (i.e. high viscosity) for LTP, which drastically reduces upon the transition to HTC (i.e. when temperature exceeds T_{HTC}). However, reducing T_{HTC} indefinitely should not necessarily reduce T_e to arbitrarily small values, because the strength of HTC also becomes quite large at intermediate depths and temperatures (e.g. 400–600 °C). For example, when T_{HTC} is equal to 600 °C in Suite 3, and the effective T_e approximately follows the 700 °C isotherm. This indicates that reducing T_{HTC} to even smaller values will not reduce the predicted T_e any further, because HTC is no weaker than LTP at temperatures less than ~700 °C. Therefore, this estimate represents a lower bound for T_e based on laboratory-derived rheology and a load with amplitude $A_0 = 3$ km and density $\rho = 3330\,\mathrm{kg\,m^{-3}}$.

In Suite 4, we test the effects of a larger load with amplitude $A_0 = 6$ km which corresponds to a normal stress consistent with the largest seamounts and ocean islands on Earth (e.g. Hawaii, Tenerife). All other aspects of the models are identical to those of Suite 1. Relative to Suite 1, the predictions of T_e from Suite 4 are smaller by 1–4 km or 1–15 per cent, and still fall between the 600–900 °C isotherms or ~25–80 km depth (Fig. 5b and Table 2). This demonstrates that the stress dependence of lithospheric rheology cannot significantly reduce estimates of T_e based on reasonable variations in load size.

In Suite 5, we test the sensitivity of T_e to the frictional coefficient of faults by reducing the frictional coefficient from $\mu_f = 0.7$ to 0.3 (Bellas & Zhong, 2021) and all aspects are consistent with Suite 1 ($A_0 = 3$ km, $T_{HTC} = 800$ °C). In Suite 5, T_e falls along the 800 °C isotherm for increasing seafloor age similar to Suites 1–4

which demonstrates a weak influence of the μ_f on T_e consistent with previous studies (Fig. 5b and Table 2, Zhong & Watts 2013). We have also tested the flexural response against the influence of non-zero cohesion equal to 75 MPa, and the influence of formulating frictional sliding to be sensitive to the differing strength of normal and reverse faults and found very weak sensitivity in both cases. It is worth noting that Zhong & Watts (2013) also found a weak influence of HTC on flexure provided the reference viscosity of the mantle is reasonable (e.g. $<10^{22}$ Pa s) and for this reason, we do not test the effects of varying HTC in this study.

In Suite 6, LTP is modified such that the activation energy, E_p, is reduced from 320 kJ mol^{-1} (Mei *et al.* 2010) to 190 kJ mol^{-1} (Fig. 2c) because previous studies have shown that flexure at Hawaii may be reproduced by laboratory-derived flow laws including that of Mei *et al.* (2010) if the activation energy for LTP, E_p, is reduced as such (e.g. Bellas *et al.* 2020). All other aspects of Suite 6 are identical to those of Suite 1. In Suite 6, T_e is reduced by a factor of approximately two compared to Suites 1–5 and falls along the ~450 °C isotherm depth, or ~10–40 km depth for seafloor age 20–130 Ma (Fig. 5b and Table 2). The significance of this result is that the only appreciable perturbation to T_e comes from a significant reduction in the strength (viscosity or yield stress) of LTP, consistent with previous studies (Zhong & Watts 2013; Bellas *et al.* 2020). Meanwhile, reasonable variations in the load amplitude A_0 (Suite 4), in the creep activation temperature T_{HTC} (Suites 1–3), or in the frictional coefficient μ_f (Suite 5), produce only minor variations in T_e.

We now introduce the global data set of observationally inferred T_e estimates, with which results from Suites 1–6 will be compared (Fig. 5a). Note that isolated seamounts and islands (e.g. Bermuda) may form by a different mechanism than those associated with hotspot tracks (e.g. Hawaii, Louisville). The observational catalogue includes 101 estimates of T_e based on flexural systems which span the global oceans, 31 of which are derived from French Polynesia (for details, refer to Watts & Zhong 2000). The vast majority of

Table 2. Infinite plate models.

Case	Thermal age (Ma)	A_0 (km)	T_{HTC} (°C)	E_{LTP} (kJ mol^{-1})	μ_f	w_0 (m)	T_e^{FE} (km)	T_e^{YSE} (km)
1a	20	3	800	320	0.7	1337	27	28
1b	30	3	800	320	0.7	1129	35	35
1c	40	3	800	320	0.7	1017	40	43
1d	50	3	800	320	0.7	933	45	48
1e	60	3	800	320	0.7	866	50	52
1f	70	3	800	320	0.7	802	56	56
1g	80	3	800	320	0.7	777	59	60
1h	90	3	800	320	0.7	733	64	63
1i	100	3	800	320	0.7	709	66	68
1j	110	3	800	320	0.7	687	70	72
1k	120	3	800	320	0.7	666	72	75
1l	130	3	800	320	0.7	647	76	78
2a	20	3	900	320	0.7	1241	30	30
2b	30	3	900	320	0.7	1057	38	42
2c	40	3	900	320	0.7	933	46	49
2d	50	3	900	320	0.7	859	51	53
2e	60	3	900	320	0.7	800	56	60
2f	70	3	900	320	0.7	750	62	65
2g	80	3	900	320	0.7	709	66	69
2h	90	3	900	320	0.7	672	72	74
2i	100	3	900	320	0.7	650	76	77
2j	110	3	900	320	0.7	630	78	81
2k	120	3	900	320	0.7	603	84	86
2l	130	3	900	320	0.7	587	86	90
3a	20	3	600	320	0.7	1551	22	18
3b	30	3	600	320	0.7	1312	28	29
3c	40	3	600	320	0.7	1162	34	32
3d	50	3	600	320	0.7	1059	38	36
3e	60	3	600	320	0.7	984	43	43
3f	70	3	600	320	0.7	923	47	45
3g	80	3	600	320	0.7	873	50	50
3h	90	3	600	320	0.7	832	54	54
3i	100	3	600	320	0.7	796	57	57
3j	110	3	600	320	0.7	765	60	60
3k	120	3	600	320	0.7	738	64	63
3l	130	3	600	320	0.7	714	66	67
4a	20	6	800	320	0.7	2892	24	26
4b	30	6	800	320	0.7	2405	32	31
4c	40	6	800	320	0.7	2143	37	38
4d	50	6	800	320	0.7	1953	43	44
4e	60	6	800	320	0.7	1806	48	51
4f	70	6	800	320	0.7	1681	53	54
4g	80	6	800	320	0.7	1607	56	59
4h	90	6	800	320	0.7	1515	62	63
4i	100	6	800	320	0.7	1462	64	66
4j	110	6	800	320	0.7	1414	68	70
4k	120	6	800	320	0.7	1367	70	74
4l	130	6	800	320	0.7	1327	74	75
5a	20	3	800	320	0.3	1430	24	24
5b	30	3	800	320	0.3	1184	32	35
5c	40	3	800	320	0.3	1056	38	39
5d	50	3	800	320	0.3	962	43	45
5e	60	3	800	320	0.3	889	49	51
5f	70	3	800	320	0.3	826	54	54
5g	80	3	800	320	0.3	792	57	59
5h	90	3	800	320	0.3	745	62	62
5i	100	3	800	320	0.3	720	66	67
5j	110	3	800	320	0.3	697	68	70
5k	120	3	800	320	0.3	675	72	74
5l	130	3	800	320	0.3	655	74	78
6a	20	3	800	190	0.7	2124	13	14
6b	30	3	800	190	0.7	1829	17	16
6c	40	3	800	190	0.7	1639	20	20

Table 2. Continued

Case	Thermal age (Ma)	A_0 (km)	T_{HTC} (°C)	E_{LTP} (kJ mol^{-1})	μ_f	w_0 (m)	T_e^{FE} (km)	T_e^{YSE} (km)
6d	50	3	800	190	0.7	1491	24	25
6e	60	3	800	190	0.7	1366	27	29
6f	70	3	800	190	0.7	1255	29	32
6g	80	3	800	190	0.7	1218	32	34
6h	90	3	800	190	0.7	1153	34	35
6i	100	3	800	190	0.7	1099	37	40
6j	110	3	800	190	0.7	1053	39	42
6k	120	3	800	190	0.7	1022	41	44
6l	130	3	800	190	0.7	987	43	45

*A_0 is the load amplitude, T_{HTC} is the activation temperature for high-temperature creep, E_{LTP} is the plastic activation energy, μ_f is the frictional coefficient, w_0 is the maximum surface flexure, T_e^{FE} is the elastic thickness based on numerical models and T_e^{YSE} is the elastic thickness based on the YSE method. Cases are organized into suites, within which only the thermal age is varied except for a few select cases marked with the symbols.

observationally inferred T_e estimates lie between the 300–600 °C isotherms, although estimates from French Polynesia are anomalous (Fig. 5a, Watts 2001; Watts & Zhong 2000). It is generally thought that the anomalously low T_e estimates derived from French Polynesia represent oceanic lithosphere that has been significantly modified by interaction with the South Pacific Isotopic and Thermal Anomaly (Smith *et al.* 1989). There is also appreciable spread in the T_e data set for standard settings (i.e. between the 300–600 °C isotherms) which may be related to the varying degrees of plume and magmatic activity at different ocean island systems, or to the methods that were used to infer T_e which span a large body of work published since 1970 (Watts & Zhong 2000). However, the general consensus is that T_e estimates excluding French Polynesia are standard, while T_e at French Polynesia is anomalous.

In comparison, for Suites 1–5, all of which include laboratory-derived LTP, the predictions exceed the standard observations of T_e by a factor of approximately 2, and observations from French Polynesia by even more. Meanwhile, the standard observations are accurately reproduced by Suite 6 which includes modified LTP. Therefore, we have demonstrated for the first time that laboratory-derived lithospheric rheology significantly overestimates T_e at most oceanic-plate interior settings, not just the Hawaiian Islands. In conclusion, we have shown that Hawaiian lithosphere is not anomalous in terms of elastic thickness (i.e. rheology, thermal structure and magmatic effects), and the conundrum that the yield stress of oceanic lithosphere appears stronger at subduction zones than ocean islands remains unsolved.

3.2 The yield stress envelope method and fully dynamic models of flexure

In this section, we test whether the YSE method reproduces T_e of fully dynamic viscoelastic loading models and examine the sensitivity of the YSE method to error in the curvature and strain rate which are required as inputs but not necessarily well constrained in observational studies. The overarching goal is to determine whether the YSE method, which was used to constrain lithospheric rheology at subduction zones (Hunter & Watts 2016), is associated with systematic error that may explain the discrepancy between the rheology of subducting lithosphere (equivalently, that derived in laboratory experiments), and that of oceanic plate interiors.

In the following, we present results from the 2-D numerical model, Case 1h, that are relevant to the YSE method. Recall that

Case 1h was previously present in Section 3.1 and has 90 Ma lithospheric thermal structure and load amplitude $A_0 = 3$ km (Figs 2, 4 and 5, and Table 2). At $t = 500\tau_M$ Case 1h is in steady state, the maximum surface flexure is $\sim$700 m, and the two-layer model which best reproduces flexure has $T_e = 64$ km (Fig. 6a). In addition, the maximum curvature is $\sim$$-10^{-8}$ m^{-1} which occurs in the trench outer-slope region (Fig. 6a) where observations from real flexure systems are most often available (Craig *et al.* 2014a). The 1-D vertical stress profile is taken at the location of maximum curvature and shows that elastic bending stresses reach $\sim$50 MPa and are truncated by frictional sliding near the surface, and by HTC below $\sim$65 km depth (Fig. 6b). LTP is not activated in the 1-D vertical stress profile because bending stresses are not large enough to intersect the yield stress of LTP (compare Fig. 6b with Fig. 2a). In other words, deformation is purely elastic except for yielding by frictional sliding and HTC near the surface and at depth, respectively, because LTP is so strong in Case 1h.

We use results from the numerical Case 1h to construct the corresponding YSE, and to determine T_e based on the YSE method in following steps. First, the YSE is constructed by predicting the yield stress of frictional sliding, which is a simple function of depth (eq. 1). Second, the average strain rate in the lithosphere while the surface is actively deflecting ($\dot{\varepsilon} = 10^{-16}$ s^{-1}, Fig. 4h) and a 90 Ma thermal structure are used to solve the yield stresses of LTP and HTC (eqs 2 and 3, respectively). Third, the maximum curvature in the flexural bulge region from Case 1h is used to predict the elastic bending stress (eq. 5). Fourth, the bending moment is given by the vertical integral of the YSE and elastic bending stresses (Fig. 6b; eq. 4). Finally, this bending moment is equated to the expression for the bending moment of a purely elastic plate (eq. 6) such that T_e can be solved. Note that the depth of the neutral plane, z_n, is constrained by the requirement that the integral of stresses above and below it cancel out.

When the YSE method is applied in this manner with inputs taken directly from Case 1h, the elastic thickness estimate is $T_e = 64$ km, which reproduces the true or numerical value of 64 km exactly (Table 2), thus validating the YSE method. This is what we expect given that the YSE constructed in this manner produces good agreement with the 1-D vertical stress profile taken directly from the numerical model, Case 1h (Fig. 6b).

We also test the sensitivity of the YSE method to error in strain rate and curvature since these parameters may be associated with significant uncertainty in observational studies. Curvature controls the slope of elastic bending stress with depth (eq. 5), while strain
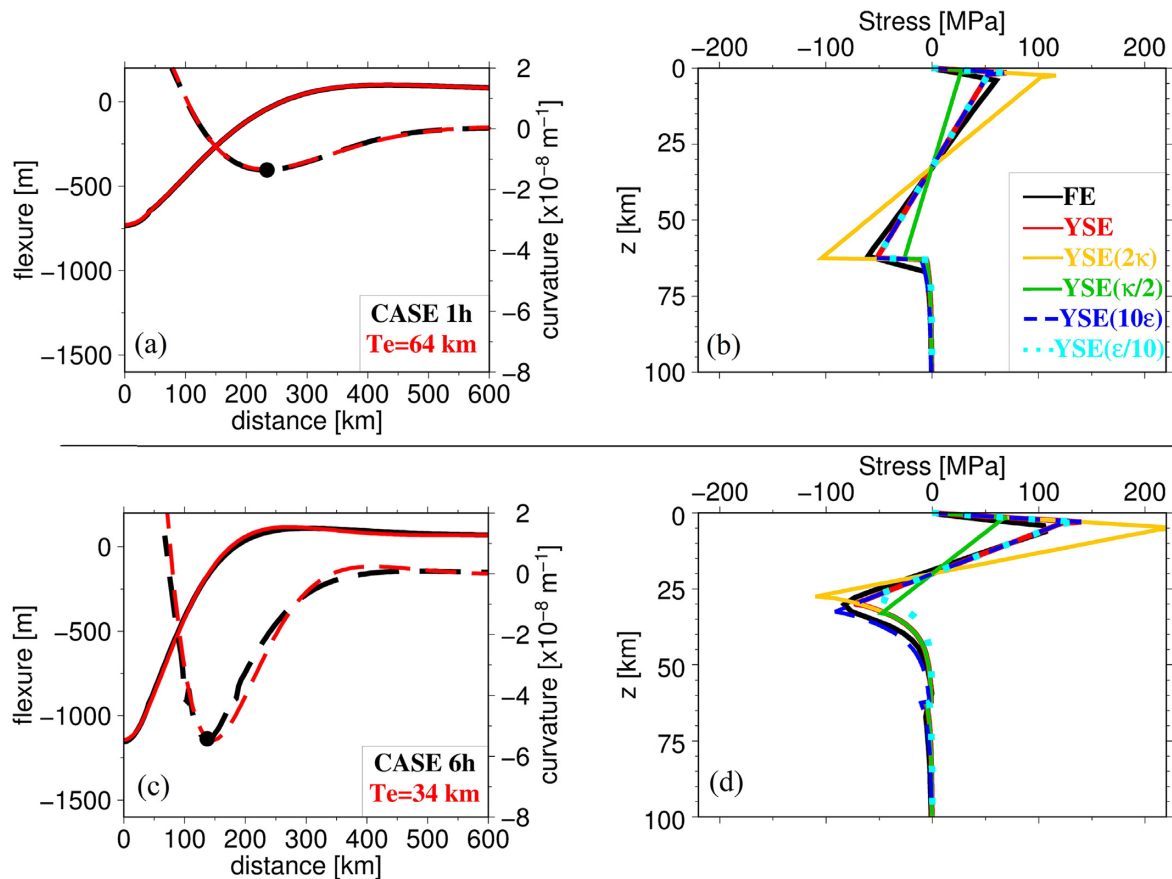
Figure 6. The YSE method and fully dynamic viscoelastic loading models. (a) The flexure (solid) and surface curvature (dashed) from Case 1h and the best-fitting two-layer model, which has $T_e = 64$ km. Only half of the flexural profile is shown, which is reflected across $x = 0$ km. The black dot marks the maximum curvature. (b) The differential stress profile taken from Case 1h at the location of maximum curvature (FE for finite element), and the stress profiles predicted by the YSE method for accurate inputs (red, YSE), for curvature that is too large by a factor of 2 (yellow, YSE(2κ)), for curvature that is too small by a factor of two (green, YSE($\kappa/2$)), for strain rate that is too large by a factor of 10 (blue, YSE($10\dot{\varepsilon}$)), and for strain rate that is too small by a factor of 10 (cyan, YSE($\dot{\varepsilon}/10$)). (c) Same as (a), but for Case 6h. (d) Same as (b) but for Case 6h.

rate controls the yield stresses of the ductile deformation mechanisms (e.g. eqs 2 and 3). First, if the curvature used as input to the YSE is increased by a factor of 2, then the slope of elastic bending stresses increases by a factor of 2, and larger bending stresses activate yielding by frictional sliding and HTC to greater degree (Fig. 6b). If the YSE method is applied as outlined above, but uses curvature that is too large by a factor of 2, then the predicted T_e is reduced from 64 to 63 km. This is because increasing the curvature is equivalent to increasing the degree of nonlinear weakening. Similarly, if curvature is reduced by a factor of 2, then the YSE method estimate of T_e increases to 70 km (Fig. 6b). This demonstrates that the YSE method applied to Case 1h is not very sensitive to error in the assumed curvature. Second, we test the sensitivity to error in the assumed strain rate. We test decreasing the strain rate from 10^{-16} to 10^{-17} s^{-1} and the effect is to decrease the yield stress of the ductile deformation mechanisms (eqs 2 and 3; Fig. 6b), such that the YSE method predicts $T_e = 63$ km. Similarly, if the strain rate is increased to 10^{-15} s^{-1}, the effect is to increase the yield stress of LTP and HTC (Fig. 6b), and the YSE method predicts $T_e = 66$ km. In summary, our results show that the YSE method is modestly sensitive to error in both strain rate and curvature in Case 1h, where error in T_e is always less than 10 per cent.

Having analysed the YSE method applied to Case 1h in some detail, we now apply the YSE method similarly to all cases in Suite

1, as well as to Suites 2–6 (Table 2). To be clear, the maximum curvature and average strain rate in the lithosphere are taken from each numerical model and used as input for each corresponding YSE and the prediction of T_e. The results are summarized in Table 2, and the main result is that the YSE method reproduces the T_e of the numerical models within ∼10 per cent errors, despite limitations such as being unable to account for spatial and temporal variations in strain rate and curvature.

Detailed results and sensitivity tests are also presented for Case 6h, for which the lithosphere is much weaker, the degree of bending is greater, and the predicted T_e is consistent with observationally inferred values for 90 Ma oceanic lithosphere (Figs 5a and 6c and d). The YSE method applied to Case 6h predicts $T_e = 37$ km compared to the fully dynamic value $T_e = 34$ km. In addition, curvature that is too large or too small by a factor of 2 causes the YSE method to predict T_e is 32 and 41 km, respectively, while strain rate that is too large (10^{-15} s^{-1}) or too small (10^{-17} s^{-1}) causes the YSE method to predict T_e is 41 or 33 km, respectively.

These results indicate that the YSE method is more sensitive to error when applied to systems with a greater degree of bending, with up to 21 per cent error associated with overestimation of T_e, but up to only 6 per cent error for underestimation. Whether the YSE method overestimates or underestimates T_e is important because significant underestimation of T_e could lead to the association of reasonable T_e

values with laboratory-derived rheology, even though our previous results suggest it is too strong (e.g. Fig. 5). However, our results show that the YSE method is not very susceptible to underestimating T_e when subject to error in the strain rate and curvature used as input.

In summary, we have tested a wide variety of loading scenarios on infinite plates which are representative of most oceanic plate interior flexure systems (Table 2). The results show that the YSE method performs well for a wide range of T_e (15–89 km), rheological parameter values (Tables 1 and 2), thermal structures (20–130 Ma), and trapezoidal load amplitudes (3–6 km) for load density $\rho = 3330$ kg m^{-3}. Furthermore, the YSE method is not particularly sensitive to error in either the curvature or the strain rate when applied to a system with modest flexure (<10 per cent error is maintained), although this sensitivity increases as the degree of flexure increases. When applied to systems subject to a significant degree of flexure (e.g. curvature $\sim 10^{-7}$ m^{-1}), the YSE method may overestimate T_e by up to 20 per cent, but underestimates T_e by no more than 6 per cent. Therefore, it seems unlikely that error from the YSE method can explain why laboratory-derived rheology, which is too strong compared to plate interior settings, appears consistent with subducting lithosphere in recent studies (Hunter & Watts 2016).

3.3 Testing the broken elastic plate model against fully dynamic models of flexure

The BEPM has been widely used to model lithospheric flexure at subduction zones (e.g. Bodine *et al.* 1981; Hunter & Watts 2016), foreland basins (Lyon-Caen & Molnar 1983), oceanic fracture zones (Wessel & Haxby 1990) and even oceanic islands (e.g. Watts & ten Brink 1989; Wessel 1993) with much success in reproducing the morphology of bending at such settings (i.e. bending with uniformly concave-downward curvature). The BEPM has recently been used in tandem with the YSE method to constrain the rheology of subducting lithosphere at circum-Pacific subduction zones (Hunter & Watts 2016). Since we demonstrated that the YSE method accurately reproduces T_e in Section 3.2, we now investigate the BEPM to test whether it is accurate and appropriate for modelling flexure at subduction zones.

In the following, we modify the viscoelastic loading model to have a reduced viscosity zone near $x = 0$ km which effectively imposes a free edge and mimics the geometry of the BEPM (e.g. Fig. 3d). The viscoelastic loading models are distinct from the BEPM in that they are subject to a finite-width load and the bending moment is not independently varied, but we suggest that the effects of a line load on the free edge of an EPM are similar. As in previous sections, we estimate T_e based on the minimum misfit two-layer model (note that the two-layer models do not include a free edge).

Case 7a with a continuous (i.e. unbroken) plate will serve as a reference model. Case 7a is identical to Case 1h except that the trapezoidal load amplitude is increased to 10 km to reflect larger loads in subduction zones (Table 3). The steady-state solution of flexure and the viscosity field are presented in Fig. 7(a), where the flexure is $\sim$2500 m and the viscosity field shows evidence of nonlinear weakening beneath the surface load (i.e. near x = 0). The two-layer model which reproduces the flexure of Case 7a with minimum misfit has $T_e = 58$ km.

Case 7b is identical to Case 7a except viscosity is reduced to 10^{21} Pa s in the lithosphere between $x = 0$ and 8 km where four elements resolve the weak zone (Figs 3d and 7b). This weak zone is imposed to simulate a free edge, the geometry of the BEPM and real Earth systems in which a free edge arises because of the existence of an adjacent weak zone. This model configuration is also similar to that of a 1-D cantilever beam that is fixed at one end. As a result of imposing this weak zone, the maximum flexure of the competent lithosphere occurs at the free edge ($\sim$3000 m, Fig. 7b), and the curvature is now uniformly concave down. The flexure of the weak zone is much greater than the competent lithosphere but will be ignored in our analysis because its only purpose is to simulate a free edge. The flexure of the competent lithosphere ($x > 20$ km) is best reproduced by a two-layer model with $T_e = 36$ km. Note that this $T_e = 36$ km is $\sim$38 per cent smaller than that of Case 7a (Table 3).

In the following, we investigate the sensitivity of the results to the properties of the weak zone. In Case 7c, the viscosity of the weak zone is increased to 10^{22} Pa s (Fig. 7c), and all other aspects of the model are identical to Case 7b. The elastic thickness $T_e = 38$ km and slightly larger than in Case 7b (36 km), which reflects the increased strength associated with the higher viscosity assigned to the weak zone (Table 3). Next, the viscosity of the weak zone is increased to 10^{23} Pa s in Case 7d, and results are presented in Fig. 7(d). The effective elastic thickness $T_e = 48$ km and significantly larger than Cases 7b and 7c (Table 3). This indicates that the flexural response of the system approaches that of the continuous plate as the viscosity of the weak zone is increased, as expected.

We also investigate sensitivity of the results to the weak zone width. In Case 7e, the weak zone width is increased from 8 to 12.5 km, but we do not present results visually because they are not significantly different from those of Case 7d (Fig. 7d). In Case 7e, the effective elastic thickness $T_e = 46$ km, indicating that a wider weak zone imparts more weakening to the system. Finally, in Case 7f, the weak zone width is increased to 19 km, and the effective elastic thickness $T_e = 44$ km, which also supports the idea that a larger weak zone imparts more weakening.

The significance of these results is that the flexural response to a load is highly sensitive to the existence of a free edge and the degree to which it is viscously coupled to the adjacent weak zone. Cases 7b–g with free edges and adjacent weak zones demonstrate a significant reduction in the net flexural strength of the whole system relative to the continuous lithosphere of Case 7a (up to 38 per cent). This indicates that the net flexural strength of the system is not only a function of the plate thickness, but also of the properties of the adjacent weak zone (i.e. free edge). Therefore, applying the

Table 3. Broken plate models.

Case	E_{LTP} (kJ mol^{-1})	T_e^{FE} (km)	η_{WZ} (Pa s)	Δx_{WZ} (km)
7a*	320	58	N/A	N/A
7b	320	36	10^{21}	8
7c	320	38	10^{22}	8
7d	320	48	10^{23}	8
7e	320	46	10^{23}	12.5
7f	320	44	10^{23}	19

*In all cases, the thermal age of the lithosphere is 90 Ma, the trapezoidal load amplitude $A_0 = 10$ km, the high-temperature creep activation temperature $T_{\mathrm{HTC}} = 800\,^\circ$C and the frictional coefficient $\mu_f = 0.7$. The viscosity of the weak zone is η_{WZ}, and the width of the weak zone is Δx_{WZ}. Case 7a is a reference model with unbroken lithosphere.
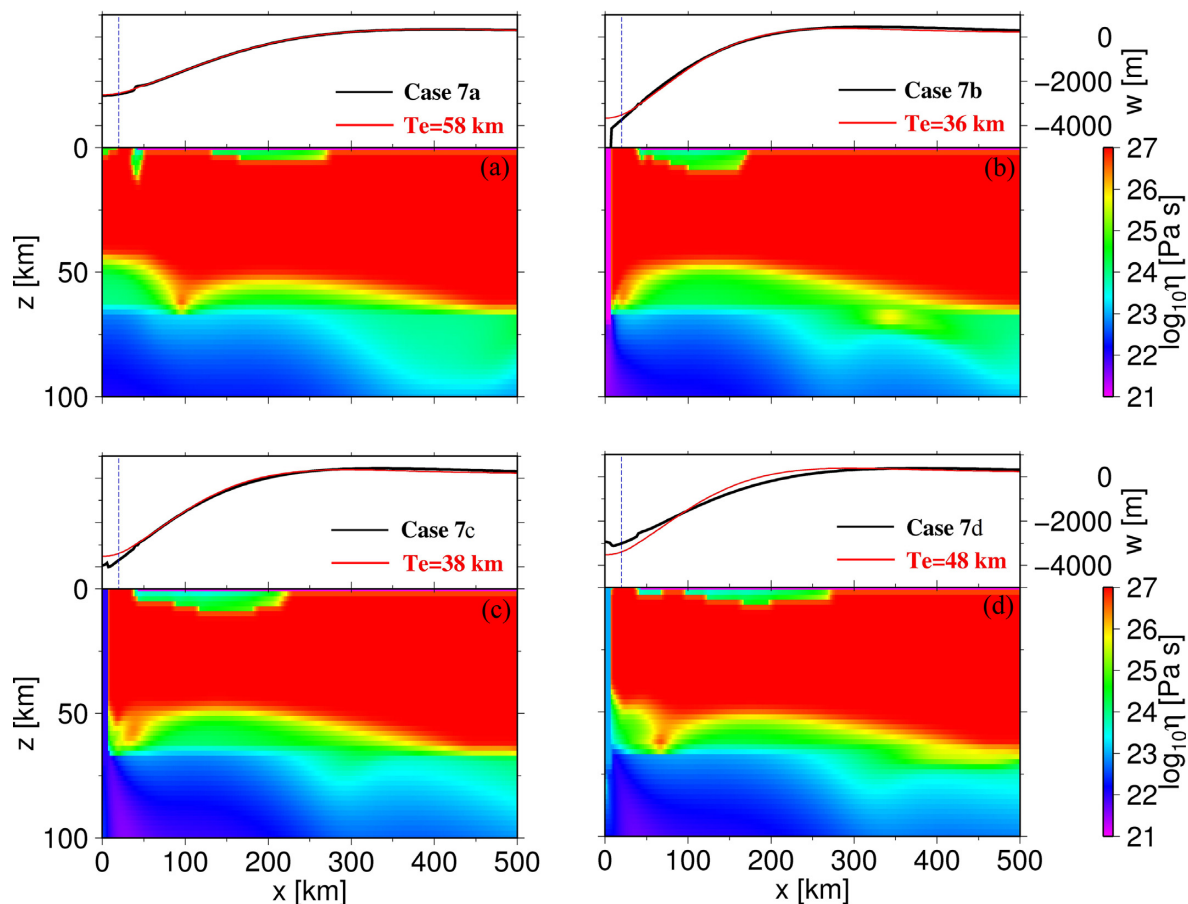
Figure 7. The effect of introducing a free edge in models of flexure. All results are symmetric across $x = 0$. (a) The steady-state flexure and viscosity field for Case 7a with infinite or continuous lithosphere (black), and the best-fitting two-layer model (red). The vertical dashed blue line shows the leftmost extent to which the misfit to flexure is calculated. (b) Similar results are presented for Case 7b which has a weak zone with viscosity 10^{21} Pa s imposed in the lithosphere between $x = 0$ and 8 km, (c) for Case 7c in which the weak zone viscosity is 10^{22} Pa s and (d) Case 7d in which the weak zone viscosity is 10^{23} Pa s. This model configuration mimics the semi-infinite geometry and free edge of the BEPM.

BEPM to a real Earth system could significantly bias the inferred plate thickness (i.e. strength and rheology). In particular, if the free edge in the model is a source of weakness relative to the real Earth system, then trade-off with the inferred plate thickness may occur to conserve the net flexural strength, where the net flexural strength is constrained by observations of flexure and loads. This could lead to overestimation of the plate strength and would have important implications for previous constraints on rheology that were based on the BEPM (e.g., Hunter & Watts 2016).

4 DISCUSSION

The distribution of stress and strain in a bending plate is of great interest because it elucidates the physical properties of the lithosphere. However, only simplified formulations of the physics of bending have been available to investigate flexural systems until quite recently. For example, the solutions of the classic EPM, BEPM and the YSE method, all rely on the thin plate approximation and other assumptions. Furthermore, deformation mechanisms including frictional sliding, LTP and HTC have been observed and quantified in mineral physics experiments, but laboratory conditions are considerably different from those in the lithosphere (e.g.

strain rate). While some recent studies (Hunter & Watts 2016) indicated that laboratory-derived rheology is consistent with the flexure of subducting lithosphere based on the BEPM and the YSE method, other studies have demonstrated that laboratory-derived rheology is too strong relative to field observations at the Hawaiian Islands (Zhong & Watts 2013; Bellas *et al.* 2020). This study seeks to understand the source of the apparent discrepancy in the yield stress of oceanic lithosphere, where oceanic lithosphere appears stronger at plate boundaries than at plate interiors, by investigating the methods that have been used to infer elastic thickness.

4.1 The yield stress envelope method and the broken elastic plate model

We show that the YSE method accurately reproduces the effective elastic thickness, T_e, to within 10 per cent error of viscoelastic loading models for a broad range of rheological parameters, thermal structures and load amplitudes (Table 2 and Fig. 6). We also show that the YSE method is not very sensitive to error in the strain rate and curvature when applied to a system with modest flexure (e.g. curvature $\sim 10^{-8}$ m^{-1}). Even for a factor of 10 error in curvature and

strain rate, T_e as estimated by the YSE method is never underestimated by more than 6 per cent. Therefore, it is not likely that the YSE method caused rheology that is actually too strong to appear consistent with observations at subduction zones by underestimating T_e in previous studies, and our investigation of the YSE method did not resolve the conundrum of strong oceanic plate boundaries relative to plate interiors.

In our investigation of the BEPM, we showed that introducing a free edge in models of flexure significantly enhances the flexural response to a load and reduces the effective T_e of the system as a whole. In addition, the degree to which the flexural response is enhanced is highly sensitive to the properties of the weak zone. The significance of this result is that the BEPM assumes a completely unconstrained free edge, but is applied to model real Earth systems that are not necessarily free to equal degree. For example, at subduction zones, the subducting plate is generally continuous, and likely maintains some finite strength and mechanical coupling to the downgoing portion of the slab as it traverses the trench and beyond. However, this finite strength is completely neglected in the BEPM which may, therefore, contain a source of weakness at the free edge relative to the real Earth system. To be clear, we are not suggesting that the continuous or infinite EPM is a better option for modelling flexure at subduction zones. Rather, we are pointing out a potentially critical difference between the BEPM and the real Earth systems to which it is applied.

If the free edge in the BEPM is weaker than the corresponding location in the real Earth system, then the BEPM will infer a higher T_e to compensate for the relative weakness of the free edge. For example, previous studies have shown that the BEPM infers a significantly larger T_e than the EPM when applied to fit observations of flexure at Hawaii (Watts & ten Brink 1989; Wessel 1993). Therefore, we suggest that exactly this type of trade-off may arise between the free edge and the inferred plate thickness in the BEPM, and if this is the case, then results from recent studies which used the BEPM to constrain lithospheric rheology at subduction zones may be called into question.

4.2 Rheology of the lithosphere at ocean island settings

We have shown that laboratory-derived rheology overestimates T_e by a factor of 2 at standard ocean island settings, and by a factor greater than 2 at French Polynesia where T_e is anomalously low (Fig. 5). We consider it highly unlikely that plume- and magmatic-activity would modify the lithosphere to equal degree at many seamounts and ocean islands, especially those with much weaker plume-activity and volcanism than that at the Hawaiian Islands (e.g. the Canary Islands, the Island of Mayotte, or Bermuda). Therefore, our new results support the conclusion of Zhong & Watts (2013) and Bellas *et al.* (2020) that laboratory-derived LTP significantly overestimates the yield stress of the Hawaiian lithosphere, and show that this conclusion also applies to oceanic lithosphere at ocean island settings in general.

Other studies (e.g. Buck *et al.* 2015; Pleus *et al.* 2020; Guest et al., 2020) have suggested that a modification to laboratory-derived rheology is not necessary, and rather that the Hawaiian lithosphere is anomalously warm and/or magmatically fractured. We acknowledge that regional thermal rejuvenation by a plume could bring laboratory-derived rheology or Suites 1–5 into agreement with observations, but that the required amount of warming corresponds to a reduction in thermal age from 60 to 20 Myr, from 100 to 30 Myr,

or ~67 per cent reduction (Fig. 5) which is not supported by observations of heat flux at the Hawaiian Islands (von Herzen *et al.* 1989) nor Cape Verde (Courtney & White 1986), swell topography at 14 ocean island settings (Huppert *et al.*, 2020), nor admittance ratios at the Hawaiian Islands (Cadio *et al.* 2012). We also acknowledge that laboratory-derived rheology could reproduce observed T_e if magmatic diking and intrusion impart a reduction in lithospheric viscosity to mantle viscosity (10^{21} Pa s) over a region that penetrates coherently through all depths in the lithosphere and over a finite width of a few kilometres and is effectively infinite in length (Cases 7a and 7b), but this is not supported by seismic observations of small isolated magma chambers and conduits (Laske *et al.* 2011; Wright & Klein 2006) nor the continuous distribution of seismicity across lithospheric depths (Klein 2016) at the Hawaiian Islands where volcanism is generally considered to be of greatest intensity on Earth.

It is also important to consider the possibility that oceanic lithosphere is always anomalous at ocean island settings at the time of loading relative to a standard oceanic lithosphere due to thermomechanical erosion by plumes and the weakening effects of magmatic plumbing systems. However, we consider it highly unlikely that such anomalies have led to a consistent factor of two reduction in T_e at most ocean island settings given the varying degrees of plume- and volcanic-activity. For example, we would expect for the greatest amount of thermal and magmatic weakening to be associated with the Hawaiian Islands, but T_e at the Hawaiian Islands is 30–35 km and slightly larger than most other estimates of T_e for 90 Ma seafloor at the time of loading (Fig. 5a).

Previous studies have demonstrated that the flexural strength of the lithosphere is primarily controlled by LTP (Zhong & Watts 2013), and we reinforce here that the only way to bring laboratory-based predictions into agreement with observations of T_e is to reduce its strength (i.e. yield stress or effective viscosity). We show that reducing the activation energy of the LTP according to Mei *et al.* (2010) from 320 to 190 kJ mol^{-1} produces agreement between predicted and observed T_e (Fig. 5).

4.3 Rheology of subducting lithosphere

Hunter & Watts (2016) reported that laboratory-derived rheology is consistent with subducting lithosphere based on the YSE method and the BEPM. This conclusion was based on an inversion which fit a uniform value of T_e to observed gravity profiles ≥ 600 km in length. However, laboratory-derived rheology is much too strong compared to Hawaiian lithosphere (Zhong & Watts 2013; Bellas *et al.* 2020) and the vast majority of ocean island settings (Fig. 5). This disagreement gives rise to a conundrum in which the rheology of subducting lithosphere appears stronger than that of plate interior settings and is a major motivation of the present study.

Based on the highly uniform composition of oceanic lithosphere, we expect that subducting lithosphere at circum-Pacific subduction zones would have equivalent rheology to the lithosphere at Hawaii and other oceanic plate interior settings, barring differences associated with size effects (Kumamoto *et al.* 2017), strain hardening (Hansen *et al.* 2019) and chemical or mechanical alteration (e.g. Huismans & Beaumont 2003; Ranero *et al.* 2003). At Hawaii, one of the largest ocean-island loads on Earth, flexure of ~5 km has accumulated over ~1 Myr (Moore & Clague 1992) which is comparable to the amount and rate of deformation at many circum-Pacific subduction zones ($\dot{\varepsilon}$~10^{-16} s^{-1}). This suggests that lithospheric rheology would be similarly affected by deformation (i.e. size effects

and strain hardening) at Hawaii compared to subduction zones, where the effects are likely saturated at both settings. In contrast, curvature at circum-Pacific subduction zones ($\sim 10^{-6}$ m^{-1}) is significantly larger than that at Hawaii ($\sim 10^{-7}$ m^{-1}) such that larger stress, greater activation of yielding mechanisms (Garcia *et al.* 2019) and a greater potential for chemical and mechanical alteration, are all associated with subducting lithosphere. This suggests that, if anything, the rheology of subducting lithosphere should be weaker than that of the oceanic plate interior, which makes it even more difficult to reconcile why laboratory-derived rheology appears consistent with subduction zones (Hunter & Watts 2016) but it too strong compared to ocean island settings (Zhong & Watts 2013). In other words, if laboratory-derived rheology is too strong at plate interior settings, we would expect it to be *much* too strong at subduction zones.

Our modelling calculations reveal that the existence of a free edge and the properties of a weak zone can significantly enhance the flexural response to a load (Figs 3d and 7). This suggests that trade-off may occur between the free edge and T_e inferred by the BEPM when it is applied to real Earth systems that do not possess an equally free edge (e.g. subducting lithosphere). Important questions arise regarding the implications of this trade-off. For example, to what degree does trade-off in the BEPM influence constraints on the rheology of subducting lithosphere? Unfortunately, we are presently unable to quantify the degree to which the BEPM overestimates T_e due to trade-off with the free edge. However, because laboratory-derived rheology is too strong compared to plate interior settings, we suggest that this newly identified trade-off may be partially responsible for the apparent agreement between laboratory-derived rheology and subducting lithosphere shown in recent studies (Hunter & Watts 2016). Furthermore, it is essential that subducting lithosphere be weaker than the plate interior because such a variation in strength is required for the formation of trenches and subduction zones and plate-like deformation. It is not sufficient that lithospheric loads be localized at plate boundaries, because the deformational response of a uniformly high yield-stress lithosphere would be diffuse, in contrast to the intense degree of localization that is observed at plate boundaries.

The problems associated with the BEPM may be far-reaching and have broad implications for understanding lithospheric rheology and how it varies between tectonic settings. For example, most estimates of T_e at plate boundaries have been derived using the BEPM (Hanks 1971; Caldwell *et al.* 1976; Parsons & Molnar 1976; McNutt & Menard 1982; Wessel & Haxby 1990; Levitt & Sandwell 1995; Hunter & Watts 2016). It is interesting to note that the BEPM has been used in trenches and fracture zones where the isotherm to which T_e corresponds is unusually high ($\sim$700 °C), despite the expectation that the lithosphere be weakest at plate boundary settings. The BEPM has also been widely used to model the flexure of foreland basins which form in front of mountain belts, including the India-Eurasian collisional system (Karner & Watts 1983; Lyon-Caen & Molnar 1983; Jordan & Watts 2005).

Flexure at subduction zones comprises a high degree of tectonic complexity ranging from the major thrust fault separating subducting and overriding plates, to mainly normal faults in the trench-outer-rise (Ranero *et al.* 2003; Ranero & Sallarès 2004), to laterally varying T_e (Hunter & Watts 2016), and high-stress activation of ductile yield mechanisms to the point of bending moment saturation (Garcia *et al.* 2019), all of which make it difficult to assess the applicability of a free edge as in the BEPM. For example, it is not clear to what degree T_e reduces as it traverses the region between the outer-rise and the trench axis and therefore to what degree the subducting lithosphere can be treated as a completely unconstrained free edge

at the trench. The properties of this reduction in T_e most likely depend on the age, curvature, fault geometry at individual subduction zones, and mechanical and chemical alteration. Furthermore, it is both challenging and necessary to represent the distributed negative buoyancy force from the subducted slab in the mantle which may ultimately be responsible for the trench and outer-rise topography (e.g. Zhong & Gurnis 1994). It is also unclear what loading effects may be associated with arc-volcanoes which often exhibit large positive gravity anomalies and are therefore at least partially supported by lithospheric stresses (Basset & Watts 2015). We suggest that fully dynamic viscoelastic models of subduction including internal loads from buoyancy will be required to reassess previous constraints on the rheological parameters at subduction zones. It will be highly instructive to test whether the modified rheological parameters that reproduce flexure at the Hawaiian Islands (e.g. Zhong & Watts 2013; Bellas *et al.* 2020), and most oceanic plate interior flexure systems (Fig. 5), also reproduce flexure at subduction zones in future studies.

At present, how to reconcile laboratory-derived rheology with flexure at subduction zones remains an open question, but LTP, specifically, appears to be too strong compared to oceanic lithosphere. This conclusion is also reflected in a recent study which employed models of flexure at subduction zones considering frictional, LTP, elastic and HTC deformation mechanisms and produced a relatively poor fit to observations at flexure-sensitive wavelengths associated with the outer-rise at the Marianas trench (Bessat *et al.* 2020). We suggest that the source of the apparent disagreement may be that the rheology of LTP varies significantly between laboratory and lithospheric conditions, or that a multivariate modification to rheological parameters is required to improve the fit to both laboratory and field observations. Other possibilities include that LTP may become decreasingly relevant with grain-size reduction (Kumamoto *et al.* 2017), strain hardening (Hansen *et al.* 2019), and/or serpentinization (Chernak & Hirth 2010), all of which likely occur at subduction zones. However, this would require a source of exorbitant weakening in the frictional sliding or HTC deformation mechanisms to compensate for the relative strengthening in LTP.

5 CONCLUSIONS

In this study, we first demonstrated that laboratory-derived rheology consistently overestimated a global catalogue of elastic thickness estimates at ocean island settings by a factor of 2. Since this discrepancy is global and consistent, we suggest that the discrepancy cannot be explained by anomalous thermal and magmatic structures, which vary significantly between different ocean island settings, though some authors have suggested this explains the discrepancy at the Hawaiian Islands. Rather, we argue that the discrepancy is caused by laboratory-derived rheology being too strong compared to the real Earth. We have also shown that the only way to bring predictions of T_e into agreement with observations is to reduce the strength of LTP (e.g. by reducing the activation energy), consistent with previous work (e.g. Bellas *et al.* 2020). A reduction in the strength of LTP is required because it controls the flexural strength of the lithosphere to first order.

Second, we have verified that the YSE method accurately reproduces T_e and stress compared to fully dynamic viscoelastic loading models ($\sim$10 per cent error). We showed that the YSE method is only modestly sensitive to error in curvature and strain rate, though this sensitivity increases with the degree of bending. We also demonstrate the type of error that arises in the EPM when the thin plate

approximation and others break down in Appendix A for especially keen readers.

Third, we have demonstrated that the flexural response to a load is significantly enhanced when a free edge is introduced to the system. This has implications for applying the BEPM to real Earth systems where a completely unconstrained free edge may not exist. Our models show that the flexural response to a load is a function of both plate strength and the properties of the free edge, such that trade-off may occur to conserve the total elastic thickness and fit the observational data.

We propose that trade-off between the free edge and T_e in the BEPM is partially responsible for the agreement between laboratory-derived rheology and subducting lithosphere in recent studies. This is particularly important in light of our new results, which show that laboratory-derived rheology is too strong compared to ocean island settings in genera. It will be important to re-assess the estimates of T_e and constraints on lithospheric rheology at subduction zones in future studies using models that incorporate more realistic subduction zone geometry, especially the continuity of the lithosphere and slab buoyancy.

ACKNOWLEDGEMENTS

DATA AVAILABILITY

The 2-D Cartesian viscoelastic loading model and a sample input file are available for download from: https://doi.org/10.6084/m9.figshare.14226716.

REFERENCES

Bassett, D. & Watts, A.B., 2015. Gravity anomalies, crustal structure, and seismicity at subduction zones: 2. Interrelationships between fore-arc structure and seismogenic behavior, *Geochem. Geophys. Geosyst.,* **16,** 1541–1576.

Bellas, A. & Zhong, S. J. 2021. Seismic strain rate and flexure at the Hawaiian Islands constrain the frictional coefficient., *Geochemistry, Geophysics, Geosystems* **22,** e2020GC009547. https://doi.org/10.1029/2020GC009547.

Bellas, A., Zhong, S.J. & Watts, A.B., 2020. Constraints on the rheology of the lithosphere from flexure of the Pacific Plate at the Hawaiian Islands, *Geochem. Geophys. Geosyst.,* **21,** e2019GC008819, doi:10.1029/2019GC008819.

Bessat, A., Duretz, T., Hetenyi, G., Pilet, S. & Schmalholz, S.M., 2020. Stress and deformation mechanisms at a subduction zone: insights from 2-D thermomechanical numerical modelling, *Geophys. J. Int.,* **221,** 1605–1625.

Billen, M.I. & Gurnis, M., 2005. Constraints on subducting plate strength within the Kermadec trench, *J. geophys. Res.,* **110**(B5), doi:10.1029/2004JB003308.

Bodine, J.H., Steckler, M.S. & Watts, A.B., 1981. Observations of flexure and the rheology of the oceanic lithosphere, *J. geophys. Res.,* **86**(B5), 3695–3707.

Buck, W.R., Lavier, L.L. & Choi, E., 2015. Magma explains low estimates of lithospheric strength based on flexure of ocean island loads, *EGU General Assembly 2015, April, Vienna, Austria.* http://ui.adsabs.harvard.edu/abs/2015EGUGA..1714525B/abstract.

Byerlee, J., 1978. Friction of rocks, *Pure appl. Geophys,* **116**(4-5), 615–626.

Cadio, C., Ballmer, M.D., Panet, I., Diament, M. & Ribe, N., 2012. New constraints on the origin of the Hawaiian swell from wavelet analysis of the geoid to topography ratio, *Earth planet. Sci. Lett.,* **359-360,** 40–54.

Caldwell, J.G., Haxby, W.F., Karig, D.E. & Turcotte, D.L., 1976. On the applicability of a universal elastic trench profile, *Earth planet. Sci. Lett.,* **31**(2), 239–246.

Chernak, L.J. & Hirth, G., 2010. Deformation of antigorite serpentinite at high temperature and pressure, *Earth planet. Sci. Lett.,* **296,** 23–33.

Courtney, R.C. & White, R.S. 1986. Anomalous heat flow and geoid across the Cape Verde Rise: evidence for dynamic support from a thermal plume in the mantle, *Geophys. J.R. astr. Soc.,* **87,** 815–867.

Craig, T.J., Copley, A. & Jackson, J., 2014a. A reassessment of outer-rise seismicity and its implications for the mechanics of oceanic lithosphere, *Geophys. J. Int.,* **197,** 63–89.

Craig, T.J., Copley, A. & Middleton, T.A., 2014b. Constraining fault friction in oceanic lithosphere using the dip angles of newly-formed faults at outer rises, *Earth planet. Sci. Lett.,* **392,** 94–99.

England, P., 2018. On shear stresses, temperatures, and the maximum magnitudes of earthquakes at convergent plate boundaries, *J. geophys. Res.: Solid Earth,* **123,** 7165–7202.

Freed, A.M., Herring, T. & Bürgmann, R., 2010. Steady-state laboratory flow laws alone fail to explain post-seismic observations, *Earth planet. Sci. Lett.,* **300,** 1–10.

Gao, X. & Wang, K., 2014. Strength of stick-slip and creeping subduction megathrusts from heat flow observations, *Science,* **345,** 1038–1041.

Garcia, E.S.M., Sandwell, D.T. & Bassett, D., 2019. Outer trench slope flexure and faulting at Pacific basin subduction zones, *Geophys. J. Int.,* **218,** 708–728.

Goetze, C. & Evans, B., 1979. Stress and temperature in the bending lithosphere as constrained by experimental rock mechanics, *Geophys. J. R. astr. Soc.,* **59,** 463–478.

Guest, I., Ito, G., Garcia, M.O. & Hellebrand, E., 2020. Extensive magmatic heating of the lithosphere beneath the Hawaiian Islands inferred from Salt Lake Crater Mantle xenoliths, *Geochem. Geophys. Geosyst.,* **21,** e2020GC009359, doi:10.1029/2020GC009359

Hager, B.H. & Richards, M.A., 1989. Long-wavelength variations in Earth's geoid: physical models and dynamical implications, *Philos. Trans. R. Soc. Lond., Ser. A,* **328,** 309–327.

Hanks, T.C., 1971. The Kuril Trench-Hokkaido Rise System: large shallow earthquakes and simple models of deformation, *Geophys. J. R. astr. Soc.,* **23**(2), 173–189.

Hansen, L.N., Kumamoto, K.M., Thom, C.A., Wallis, D., Durham, W.B. & Goldsby, D.L., 2019. Low-temperature plasticity in olivine: grain size, strain hardening, and the strength of the lithosphere, *J. geophys. Res.,* **124,** 5427–5449.

Hirano, N., Koppers, A.A.P., Takahashi, A., Fujiwara, T. & Nakanishi, M., 2008. Seamounts, knolls and petit-spot monogenetic volcanoes on the subducting Pacific plate, *Basin Res.,* **20,** 543–553.

Hirth, G. & Kohlstedt, D.L., 2003. Rheology of the upper mantle and the mantle wedge: a view from the experimentalists, in *Inside the Subduction Factory, Geophysical Monograph,* vol. **138,** edited by Eiler, J., pp. 83–105, AGU, Washington, DC.

Huismans, R.S. & Beaumont, C., 2003. Symmetric and asymmetric lithospheric extension: relative effects of frictional-plastic and viscous strain softening, *J. geophys. Res.,* **108,** B10, 2496, doi:10.1029/2002JB002026.

Hunter, J. & Watts, A.B., 2016. Gravity anomalies, flexure, and mantle rheology seaward of circum-Pacific trenches, *Geophys. J. Int.,* **207,** 288–316.

Huppert, K.L., Perron, J.T. & Royden, L.H. 2020. Hotspot swells and the lifespan of volcanic ocean islands, *Sci. Adv.,* **6,** eaaw6906.

Idrissi, H., Bollinger, C., Boioli, F., Schryvers, D. & Cordier, P. 2016. Low-temperature plasticity of olivine revisited with in situ TEM nanomechanical testing, *Sci. Adv.,* **2,** e1501671.

Jordan, T.A. & Watts, A.B. 2005. Gravity anomalies, flexure and the elastic thickness structure of the India–Eurasia collisional system, *Earth and Planetary Science Letters,* **236,** 732–750.

Karato, S.-I. & Wu, P., 1993. Rheology of the upper mantle, *Science,* **260,** 771–778.

Karato, S.I., 2012. Rheological properties of minerals and rocks, *Physics and Chemistry of the Deep Earth,* Wiley-Blackwell.

Karner, G.D. & Watts, A.B., 1983. Gravity anomalies and flexure of the lithosphere at mountain ranges, *J. geophys. Res.,* **88**(B12), 10449–10477.

Klein, F. W., 2016. Lithospheric flexure under the Hawaiian volcanic load: Internal stresses and a broken plate revealed by earthquakes, *J. Geophys. Res. Solid Earth,* **121,** 2400–2428. doi:10.1002/2015JB012746

Kumamoto, K.M., Thom, C.A., Wallis, D., Hansen, L.N., Armstrong, D.E.J. & Warren, J.M., 2017. Size effects resolve discrepancies in 40 years of work on low-temperature plasticity in olivine, *Sci. Adv.,* **3**(9), e1701338, doi:10.1126/sciadv.1701338.

Laske, G., *et al.* 2011. Asymmetric shallow mantle structure beneath the Hawaiian Swell—evidence from Rayleigh waves recorded by the PLUME network, *Geophys. J. Int.,* **187,** 1725–1742.

Levitt, D.A. & Sandwell, D.T., 1995. Lithospheric bending at subduction zones based on depth soundings and satellite gravity, *J. geophys. Res.,* **100**(B1), 379–400.

Lyon-Caen, H. & Molnar, P., 1983. Constraints on the structure of the Himalaya from an analysis of gravity anomalies and a flexural model of the lithosphere, *J. geophys. Res.,* **88**(B10), 8171–8191.

McNutt, M., 1984. Lithospheric flexure and thermal anomalies, *J. geophys. Res.,* **89**(B13), 11180–11194.

McNutt, M.K. & Menard, H.W., 1982. Constraints on yield strength in the oceanic lithosphere derived from observations of flexure, *Geophys. J. Int.,* **71**(2), 363–394.

Mei, S., Suzuki, A.M., Kohlstedt, D.L., Dixon, N.A. & Durham, W.B., 2010. Experimental constraints on the strength of the lithospheric mantle, *J. geophys. Res.,* **115**(B8), doi:10.1029/2009JB006873.

Mitrovica, J. & Forte, A.M., 1997. Radial profile of mantle viscosity: results from the joint inversion of convection and postglacial rebound observables, *J. geophys. Res.,* **102,** 2751–2769.

Moore, J.G. & Clague, D.A., 1992. Volcano growth and evolution of the island of Hawaii, *Bull. geol. Soc. Am.,* **104,** 1471–1484.

Mueller, S. & Phillips, R.J., 1995. On the reliability of lithospheric constraints derived from models of outer-rise flexure, *Geophys. J. Int.,* **123**(3), 887–902.

Parsons, B. & Molnar, P., 1976. The origin of outer topographic rises associated with trenches, *Geophys. J. Int.,* **1**(4), 707–712.

Pleus, A., Ito, G., Wessel, P. & Frazer, L.N., 2020. Rheology and thermal structure of the lithosphere beneath the Hawaiian Ridge inferred from gravity data and models of plate flexure, *Geophys. J. Int.,* **222,** 207–224.

Podolefsky, N.S., Zhong, S.J. & McNamara, A.K., 2004. The anisotropic and rheological structure of the oceanic upper mantle from a simple model of plate shear, *Geophys. J. Int.,* **158,** 287–296.

Ranero, C.R., Morgan, J.P., McIntosh, K. & Reichert, C., 2003. Bending-related faulting and mantle serpentinization at the Middle America trench, *Nature,* **425,** 367–373.

Ranero, C.R. & Sallarès, V., 2004. Geophysical evidence for hydration of the crust and mantle of the Nazca plate during bending at the north Chile trench, *Geology,* **32**(7), 549–552.

Ribe, N.M. & Christensen, U.R., 1994. 3-Dimensional modeling of plume-lithosphere interaction, *J. geophys. Res.,* **99,** 669–682.

Smith, W.H.F., Staudigel, H., Watts, A.B. & Pringle, M.S., 1989. The Magellan Seamounts: early Cretaceous Record of the South Pacific isotopic and thermal anomaly, *J. geophys. Res.,* **94**(B8), 10,501–510-523.

Turcotte, D.L. & Schubert, G., 1982. *Geodynamics: Applications of Continuum Physics to Geological Problems,* John Wiley & Sons, 450pp.

Von Herzen, R.P., Cordery, M.J., Detrick, R.S. & Fang, C., 1989. Heat flow and the thermal origin of hot spot swells: the Hawaiian swell revisited, *J. geophys. Res.,* **94**(B10), 13783–13799.

Watts, A.B., 2001. *Isostasy and Flexure of the Lithosphere,* Cambridge Univ. Press.

Watts, A.B. & Burov, E.B., 2003. Lithospheric strength and its relationship to the elastic and seismogenic layer thickness, *Earth planet. Sci. Lett.,* **213,** 113–131.

Watts, A.B., Grevemeyer, I., Shillington, D.J., Dunn, R.A., Boston, B. & Gomez de la Pena, L., 2021. Seismic structure, gravity anomalies and flexure along the Emperor Seamount chain. *J. geophys. Res.: Solid Earth,* **126,** e2020JB021109, doi:10.1029/2020JB021109

Watts, A.B. & ten Brink, U.S., 1989. Crustal structure, flexure, and subsidence history of the Hawaiian Islands, *J. geophys. Res.,* **94,** 10473–10500.

Watts, A.B. & Zhong, S. 2000. Observations of flexure and the rheology of oceanic lithosphere, *Geophys. J. Int.,* **142,** 855–875.

Wessel, P., 1993. A Reexamination of the Flexural Deformation Beneath the Hawaiian Islands, *J. geophys. Res.,* **98,** 12177–12190.

Wessel, P. & Haxby, W., 1990. Thermal stresses different subsidence, and flexure and oceanic fracture zones, *J. geophys. Res.,* **95**(B1), 375–391.

Wright, T.L. & Klein, F.W. 2006. Deep magma transport at Kilauea volcano, *Hawaii, Lithos,* **87,** 50–79.

Zhong, S.J., 1997. Dynamics of crustal compensation and its influences on crustal isostasy, *J. geophys. Res.,* **102,** 15287–15299.

Zhong, S.J. & Gurnis, M., 1994. Controls on trench topography from dynamic models of subducted slabs, *J. geophys. Res.,* **99**(B8), 15683–15695.

Zhong, S.J., Paulson, A. & Wahr, J., 2003. Three-dimensional finite element modeling of Earth's viscoelastic deformation: effects of lateral variations in lithospheric thickness, *Geophys. J. Int.,* **155,** 679–695.

Zhong, S.J. & Watts, A.B., 2002. Constraints on the dynamics of mantle plumes from uplift of the Hawaiian Islands, *Earth planet. Sci. Lett.,* **203,** 105–116.

Zhong, S.J. & Watts, A.B., 2013. Lithospheric deformation induced by loading of the Hawaiian Islands and its implications for mantle rheology, *J. geophys. Res.,* **118**(11), 6025–6048.

APPENDIX A: BREAKDOWN OF THE THIN PLATE APPROXIMATION

In this appendix, we investigate the type of error that arises in the EPM when the thin plate approximation becomes decreasingly valid. This occurs when the wavelength of the load becomes comparable to the thickness of the plate (i.e. $\lambda >> T_e$ becomes invalid). This is accomplished by comparing predictions from the EPM with the fully dynamic viscoelastic loading model which does not depend on the thin plate approximation (Section 2.3 in the main text).

The model domain is 1500 km wide (x) and 600 km deep (z), and the surface load is expressed as a sinusoidal function of horizontal position x

$$\sigma_0(x) = \rho g A_0 \cos\left(\frac{2\pi x}{\lambda}\right), \tag{A1}$$

in which ρ is the mantle density. For all models in the appendix, $A_0 = 3$ km is the load amplitude, the load is constant in time and the viscosity structure is two-layer with a high-viscosity layer thickness of 50 km (Fig. A1). All other model parameters are given in Table 1.

In Case 0a, the wavelength of the load $\lambda = 3000$ km which is much larger than $T_e = 50$ km. Therefore, Case 0a will serve as a reference model in which we expect excellent agreement between the fully dynamic model and the EPM. The time-dependent deformational response is computed for 1000 time steps or 250 Maxwell times based on mantle viscosity ($\tau_M = \eta_0/\mu \sim 950$ yr). The evolution of surface flexure and stress are shown at $t = 0$ (Figs A2a and b), $t = 12.5\tau_M$ (Figs A2c and d) and $t = 250\tau_M$ (Figs A2e and f).

At $t = 0$, the deformational response is purely elastic, and the amplitude of surface flexure is < 500 m. After $12.5\tau_M$, the amplitude of surface deflection has increased to > 2000 m, stresses up to 100 MPa begin to concentrate in the lithosphere, and strain rates of 10^{-15} s^{-1} begin to concentrate in the weak underlying mantle. After $250\tau_M$, the surface flexure is sinusoidal with amplitude $w_0 = 2997.7$ m which almost fully compensates the surface load (Fig. A2e), stresses in the weak underlying mantle have
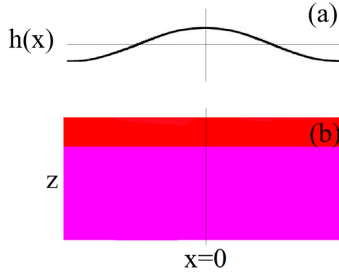
Figure A1. Model schematic. The models in this appendix are identical to those in the main text, except for the load which is sinusoidal. We consider only two-layer models in this section, and models are symmetric across $x = 0$.

fully relaxed (Fig. A2f) and the system is in steady state. Stresses in the lithosphere decrease between $12.5\tau_M$ and $250\tau_M$ possibly because the load becomes almost fully compensated such that the forcing from a horizontal gradient in topography is removed. Near-complete compensation of a long-wavelength load is consistent with analytical solutions of viscoelastic loading (e.g. Zhong 1997).

The flexure of Case 0a agrees almost identically with the prediction from the EPM for $T_e = 50$ km and the same load (Turcotte & Schubert 1982), which also predicts a sinusoidal surface displacement with the same amplitude of $w_0 = 2997.6$ m for the elastic plate parameters used here (Fig. A3a). The curvature from both models is also sinusoidal with amplitude 1.31×10^{-8} m^{-1} and in good agreement with each other. Note that the curvature predicted by the EPM is expressed $\kappa = d^2w/dx^2 = w_0(2\pi/\lambda)^2$ (Fig. A3a). Numerical error at the domain boundaries is associated with computing the second order derivative of displacement which is less accurate than the displacement itself.

In Case 0a, it is also possible to investigate internal or depth-dependent curvature within the lithosphere although curvature is treated as constant in depth in the EPM (Figs A3b and c). Curvature from Case 0a is constant in depth near the domain edge as well as near the domain centre (Figs A3b and c for horizontally averaged curvatures at $x = 50$–300 and 750–1000 km, respectively, marked by circles in Fig. A3a). Constant curvature with respect to depth affirms that variations in depth are negligible for long-wavelength loads compared to plate thickness, consistent with the thin plate approximation and the EPM.

The stress from Case 0a is compared with stress predicted by the EPM at the same two locations where curvature is averaged (i.e. Figs A3d and e for horizontally averaged between $x = 50$–300 and 750–1000 km, respectively). For Case 0a, the deviatoric normal stresses are equal and opposite ($\tau_{xx} = -\tau_{zz}$), the deviatoric shear stress is small ($\tau_{xz} \sim 0$), and the differential stress is twice the deviatoric normal stress ($\tau_{xx} - \tau_{zz} = 2\tau_{xx}$) (Figs A3d and e), as expected for an incompressible medium with $du_x/dx = -du_z/dz$ (i.e. eq. 7) and constant viscosity. The EPM prediction σ_{xx} agrees well with the differential stress from Case 0a $\tau_{xx} - \tau_{zz}$ because the thin plate approximation assumes $\sigma_{zz} = 0$ at the surface and throughout the plate, such that σ_{xx} is equal to the differential stress (i.e. $\sigma_{xx} = \sigma_{xx} - \sigma_{zz} = \tau_{xx} - \tau_{zz}$). Note that σ_{xx} from the EPM is a total stress component (i.e. including the hydrostatic component), whereas our numerical model predicts deviatoric stresses.

The deviatoric components of stress based on the EPM are derived in the following to show they also agree with those in the fully dynamic model (Figs A3d and e). The hydrostatic component of stress in the EPM is expressed—$P = 1/3(\sigma_{xx} + \sigma_{yy} + \sigma_{zz})$ which can be rewritten—$P = \sigma_{xx}(1+\nu)/3$ since $\nu\sigma_{yy} = \sigma_{xx}$ and $\sigma_{zz} = 0$ (Turcotte & Schubert 1982). Removing the hydrostatic component from the total stresses produces the deviatoric stress components according to the EPM,

$$\tau_{xx} = \frac{2-\nu}{3}\sigma_{xx}, \tag{A2}$$

$$\tau_{zz} = -\frac{2-\nu}{3}\sigma_{xx}, \tag{A3}$$

$$\tau_{yy} = \frac{2\nu-1}{3}\sigma_{xx}. \tag{A4}$$

Since incompressibility is imposed in the numerical models, we let $\nu = 0.5$ in the EPM as well. It is worth noting that while incompressibility is equivalent to $\nu = 0.5$, most crustal and mantle rocks are Poisson solids, for which $\nu \sim 0.3$, but we do not expect this difference to significantly alter the results. The deviatoric stress components from the EPM are thus $\tau_{xx} = \sigma_{xx}/2$, $\tau_{zz} = -\sigma_{xx}/2$ and $\tau_{yy} = 0$, all of which are identical to the fully dynamic numerical solutions (Figs A3d and e). Finally, we note that the total stress σ_{xx} and not the deviatoric normal stress τ_{xx} should be integrated to solve the bending moment because all forces related to bending are encapsulated in σ_{xx} but not τ_{xx} (eqs 4 or 6).

Next, in Case 0b, we investigate the type of error that arises in the EPM for a load wavelength comparable to the plate thickness. The wavelength of the load is reduced by a factor of 10 relative to Case 0a such that $\lambda = 300$ km, the horizontal model domain is reduced to 150 km, and all other aspects of Cases 0a and 0b are identical. The surface flexure and curvature are sinusoidal with amplitudes 406.6 m and 1.75×10^{-7} m^{-1}, respectively (Fig. A3f). Internal curvature of the lithosphere varies appreciably with depth in contrast to Case 0a, both near the domain edge at $x = 5$–30 km (Fig. A3g) and near the domain centrer at $x = 75$–100 km (Fig. A3h). We also note that the depth-averaged internal curvature is greater in magnitude than the surface curvature regardless of whether the flexure is concave-up (Fig. A3g) or concave-down (Fig. A3h). We suggest that vertical variation of curvature within the plate may be one manifestation of the breakdown of the thin plate approximation. Stresses are approximately an order of magnitude larger compared with Case 0a, and the shear stress τ_{xz} increases especially at mid-plate depths (Figs A3i and j).

In comparison, the EPM predicts the amplitudes of deflection and curvature are 332.4 m and 1.46×10^{-7} m^{-1}, both of which are underestimates compared to the numerical results (Fig. A3f) and overestimates the differential stress (Figs A3i and j). If we consider the fact that the EPM overestimates the numerical stress based on the surface curvature taken from the numerical Case 0b, which is smaller in magnitude at the surface than the plate interior, then this demonstrates that vertical variations in curvature are not the only manifestation of thick plate effects, because curvature smaller than the depth-averaged value alone would cause the EPM to underestimate elastic bending stresses. Therefore, we show that at short wavelengths, breakdown of the thin plate approximation is manifested in the EPM by overestimation of bending stresses in addition
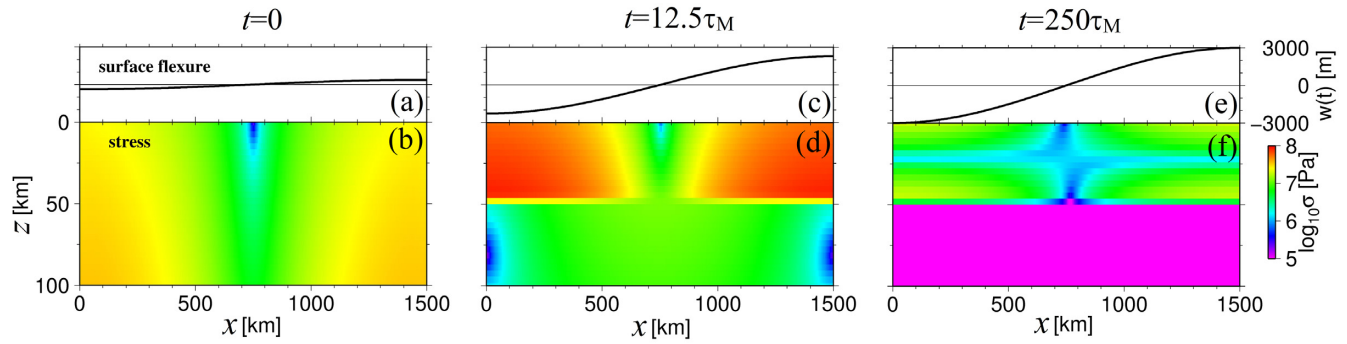
Figure A2. Time evolution of two-layer viscosity model Case 0a. The surface deflection and the stress field for varying time in response to a sinusoidal load. (a) and (b) At $t = 0$, the response is entirely elastic such that stress is distributed relatively evenly in depth. (c) and (d) At $t = 12.5\tau_M$, viscous relaxation causes stress to concentrate in the high-viscosity layer. (e) and (f) At $t = 250\tau_M$, the system is in steady state, elastic stresses are concentrated in the high-viscosity layer and the flexure is maximal.

to underestimation of surface flexure and curvature. Understanding the type of error that arises when the thin plate approximation breaks down may help to inform the kind of limits that may be placed on short-wavelength deformation in the EPM in future studies.

In summary, we have shown that the EPM predicts flexure, curvature and stress identical to that in fully dynamic viscoelastic loading models when the thin plate approximation and others are valid. However, the agreement degrades as the thin plate approximation breaks down, as is expected, and the disagreement is such that the EPM underestimates flexure and curvature, but overestimates stress relative to the fully dynamic numerical model. The thin plate

approximation is the assertion that the depth to the neutral surface is fixed, does not vary, that no vertical variations in stress (σ_{zz}, σ_{xz}) or curvature (κ) occur in the bending lithosphere, and the EPM relies on it and other assumptions such as small curvature and small angle approximations. It is not straightforward to identify which approximation leads to the error we observe in this study, or why the error has the sign configuration observed herein. However, understanding the behavior that arises when the approximations become decreasingly valid may help inform the limits that can be placed on flexural dynamics (i.e. upper and lower bounds on flexure, stress, curvature) in future studies which use the EPM.
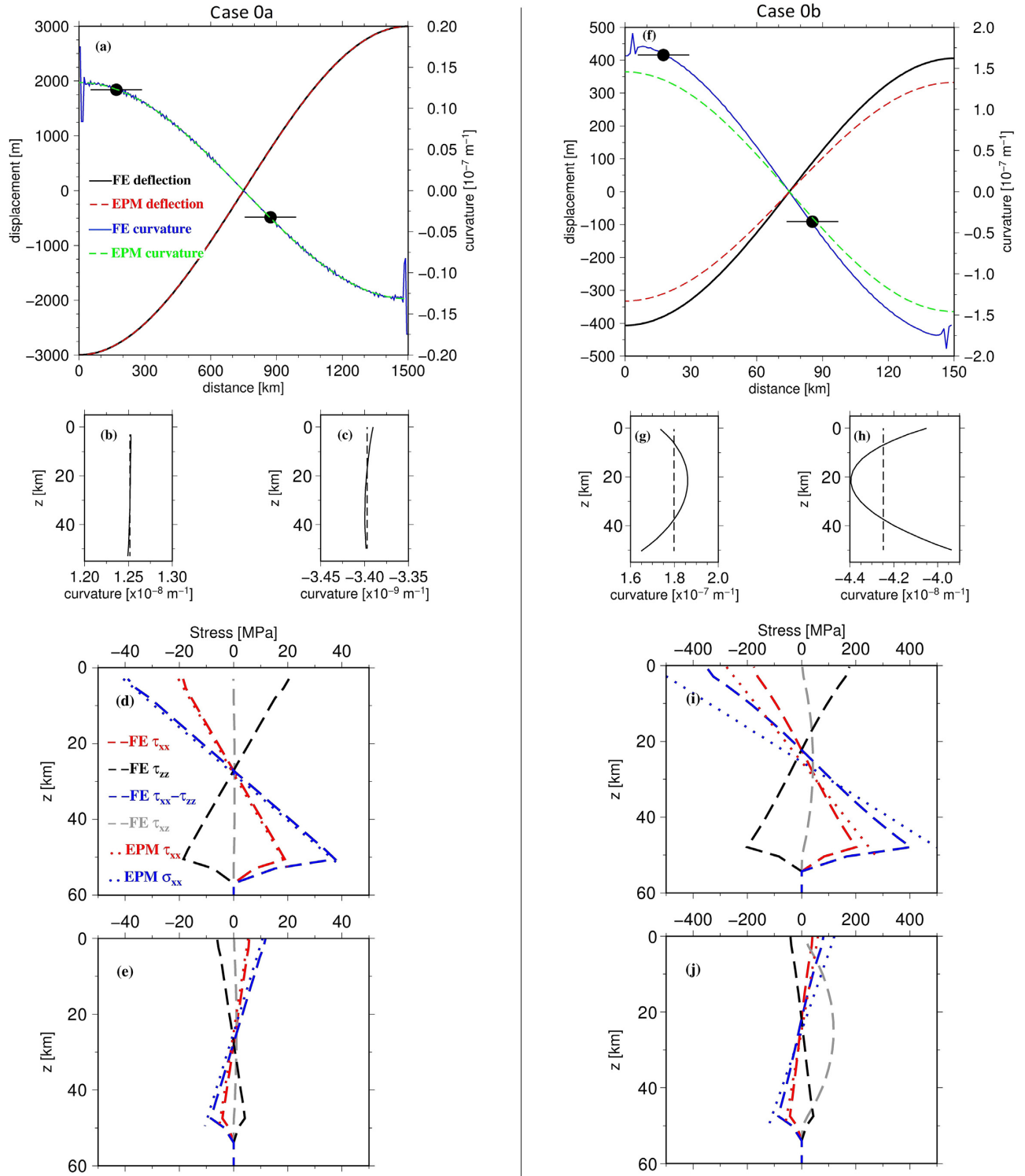
Figure A3. Comparison of predictions from the EPM and the fully dynamic model. In the left-hand column (a)–(e) are results from Case 0a which is subject to a 3000 km wavelength load. On the right (f)–(j) are results from Case 0b which is subject to a 300 km wavelength load. From top to bottom, we present the surface deflection and surface curvature (a, f); (solid) the internal or depth-dependent curvature which is horizontally averaged over the ranges (bars) centred on circles in (a) and (f), and (dashed) the vertical average (b) and (c), (g) and (h); (dashed) the numerical or FE vertical stress profiles averaged near the domain edge marked by leftmost circles in (a) and (f), and (dotted) the EPM prediction (d) and (i); finally, (dashed) the numerical (FE) vertical stress profiles averaged near the domain centre marked by central circles in (a) and (f), and (dotted) the EPM prediction (e) and (j). In the legend for stress profiles, τ represents deviatoric stress, and σ represents total stress.